A LONG-WAVELENGTH QUANTUM DOT-CONCENTRIC FÖRSTER RESONANCE ENERGY TRANSFER CONFIGURATION: CHARACTERIZATION AND APPLICATION IN A MULTIPLEXED HYBRIDIZATION ASSAY

by

Jia Jun Li

B. Sc., The University of British Columbia, 2014

A THESIS SUBMITTED IN PARTIAL FULFILLMENT OF THE REQUIREMENTS FOR THE DEGREE OF

MASTER OF SCIENCE

in

The Faculty of Graduate and Postdoctoral Studies

(Chemistry)

THE UNIVERSITY OF BRITISH COLUMBIA

(Vancouver)

July 2017

Abstract

Concentric Förster resonance energy transfer (cFRET) based on fluorescent quantum dots as nanoscaffolds is a promising strategy for multiplexed bioanalysis and bioimaging. To expand the scope of prototypical cFRET strategy, which was limited to a particular combination of quantum dot (QD), peptides and fluorescent dyes, work in this thesis adopted a combination of an orange-emitting QD605 and red/deep-red fluorescent dyes Alexa Fluor 633 and Alexa Fluor 680 for the design of a long-wavelength cFRET configuration. This new configuration has shown certain superior properties compared to the prototypical one. Although more susceptible to photobleaching, the long-wavelength cFRET configuration offers much higher signal-to-background ratios in biological samples due to both the excellent brightness of the orange-emitting QD605 and long-wavelength excitation and emission. A rate analysis of both of the competitive and sequential energy transfer pathways revealed the dominant competitive pathway in the long-wavelength cFRET configuration, contrary to a dominant sequential pathway in the prototypical configuration. Moreover, to expand cFRET beyond peptide-linked configurations, an oligonucleotide-linked cFRET configuration was constructed and used to demonstrate the multiplexed detection of unlabeled target oligonucleotides through efficient toehold-mediated strand displacement. Overall, work in this thesis has contributed to evidence of cFRET as a general strategy and expanded it to a wider range of applications.

Lay Abstract

This thesis presents a detection platform called cFRET (concentric Förster resonance energy transfer) built from fluorescent nanoparticles called quantum dots (QDs) and two organic fluorescent dyes. It can be used for the simultaneous detection and quantification of two DNA fragments. The properties of this newly designed platform that operates in the red region of the visible electromagnetic spectrum were studied and compared to a conventional configuration in the green region of the spectrum. The new red configuration demonstrates both advantages and disadvantages compared to the green configuration. The red configuration is superior in terms of greater brightness and better signal acquisition in biological media, although it is more susceptible to photobleaching in microscope imaging. Through studies of energy transfer dynamics between the quantum dot and the two dyes, it is found that the new configuration obeys the theoretical framework that governs in the conventional configuration, but with differences in the balance of how the two dyes interact with the quantum dot. Overall, this new design of red cFRET strategy is an improved step towards wider applications of cFRET in bioanalysis.

Preface

The research presented in Chapters 2 and 3 of this thesis has been published:

Li, J.J. and W.R. Algar, "A long-wavelength quantum dot-concentric FRET configuration: characterization and application in a multiplexed hybridization assay." *Analyst*, 2016. **141**(12): p. 3636-3647.

I co-designed and independently executed the experiments, most data analysis, and wrote the thesis. My supervisor, Dr. Russ Algar, co-designed the research and helped with the interpretation and discussion of the results. He also provided feedback and editing assistance with the thesis. Dr. Algar led the data analysis for the photobleaching, biological serum and blood and fluorescence lifetime measurements, and I executed all of these experiments.

Table of Contents

List of tables

List of figures

List of symbols and abbreviations

A633	Alexa Fluor 633
A680	Alexa Fluor 680
AHA	6-aminohexanoic acid
AO	Atomic orbitals
Blk	Block (strand)
BOI	Biomolecule of interest
BRET	Bioluminescence resonance energy transfer
cFRET	Concentric Förster resonance energy transfer
CRET	Chemiluminescence resonance energy transfer
Cy3	Cyanine 3
Cy5	Cyanine 5
DCM	Dichloromethane
DHLA	Dihydrolipoic acid
DIC	Diisopropyl carbodiimide
DMF	Dimethyl formamide
DMSO	Dimethyl sulfoxide
DOS	Density of states
dsDNA	Double stranded deoxyribonucleic acids
DTL	Dithiol-terminated linker
EDC	1-Ethyl-3-(3-dimethylaminopropyl)carbodiimide
ESI-MS	Electrospray ionization – mass spectrometry
EtOH	Ethanol
FRET	Förster resonance energy transfer
FWHM	full-width-at-half-maximum
GSH	Glutathione
HOMO	Highest occupied molecular orbital
LOD	Limit of detection
LUMO	Lowest unoccupied molecular orbital
MAA	Mercaptoacetic acid
MBP	Maltose binding protein
MeCN	Acetonitrile
MeOH	Methanol
MO	Molecular orbitals
NHS	*N*-hydroxysuccinimide
Ni-NTA	Ni^{2+}-nitrilotriacetic acid
NIR	Near-infrared
nt	Nucleotide
PBS	Phosphate buffered saline

PCR	Polymerase chain reaction
PEG	Polyethylene glycol
Pep	Peptide
PL	Photoluminescence
Py	Pyridine
QD	Quantum dot(s)
RNA	Ribonucleic acid
SEC	Size exclusion chromatography
SMCC	succinimidyl-4-(N-maleimidomethyl)cyclohexane-1-carboxylate
TCEP	tris(2-carboxyethyl)phosphine
TEAA	Triethylamine acetate
Tgt	Target (strand)
THF	Tetrahydrofuran
TMAH	Tetramethylammonium hydroxide
TOP/TOPO	Trioctylphosphine/trioctylphosphine oxide
UV	Ultraviolet

Acknowledgements

I would like to first thank Dr. Russ Algar for his efforts and time on supervising me with guidance, patience, encouragements and understanding, especially when experiments did not go as expected. I would also like to thank Melissa Massey and Eleonora Petryayeva for their help and advice on my project. I am grateful for Saeid Kamal for his patient advice on the use of laser facility at UBC. Thanks Jae-Seung Lee for helping with preparation of blind trial with unknown samples. Thanks to other group members Erin Conroy, Kelsi Lix, Michael Tran, and David Kim for help and fun in the lab.

I would also like to thank all the professors who have taught me in the past at UBC, and from whom my knowledge in chemistry came. I would like to extend special thanks to the NanoMat program for offering a series of opportunities on internships, courses and workshops. I appreciate the knowledge and especially the learning skills from Dr. Mark MacLachlan and Dr. Wolf's NanoMat courses. Thank you to NSERC for funding such a great program.

Finally, I would like to thank my family for supporting me all these years while I was obtaining my education.

Chapter 1
Introduction

The emergence of nanoparticles as a new type of material featuring particle size at the nanometer (10^{-9} m) scale has brought about numerous applications in bioanalysis. These applications take advantage of the unique optical, electronic, physical and chemical properties of nanomaterials, as well as the enhanced surface area for functionalization.[1] Among the various types of nanomaterials, interest in quantum dots for bioanalysis has emanated since photoluminescent quantum dots were first made water-soluble, which opened the door to useful applications in cellular imaging and numerous emerging applications in bioanalysis since. [2]

1.1 Introduction to quantum dots

Nanomaterials have attracted tremendous interest in all fields of science because of their unique electrical, mechanical, thermal and optical properties. Quantum dots, being one of the most widely explored nanomaterials, have proved to be an outstanding material in bioanalysis because of their special and advantageous optical properties. This chapter introduces quantum dots in terms of their size and composition, typical synthetic routes, photophysical properties, and bioanalytical applications.

1.1.1 What are quantum dots?

Quantum dots (QDs) are semiconductor nanocrystals with diameters between 2-10 nm. Every particle is a cluster of 100–1000 atoms arranged in a crystal lattice with facets. Though with facets, QDs are often drawn and approximated as spheres.[3] Synthetic methods of QDs can be categorized as top-down and bottom-up syntheses. Top-down synthesis produces nano-sized quantum dots by "cutting" a bulk material into pieces using a beam of highly energetic particles, such as in electron beam lithography, focused ion beam milling, and reactive ion etching.[4] However, QDs produced in a top-down manner are not ideal for bioanalytical applications, due to impurities present, the inhomogeneity in sizes, low yield and high cost. One of the most explored methods of

bottom-up synthesis is pyrolysis of molecular precursors leading to nucleation and growth of nanocrystals. Such QDs are typically made from Group II organometallic precursors and Group VI elements in non-polar solvent at high temperature, in the presence of trioctylphosphine/ trioctylphosphine oxide (TOP/TOPO) or other surfactants. Such methods produce QDs with good control over size through well-controlled growth conditions that include reaction time and temperature.[4] Being able to produce QDs with controlled size and in significant amounts opened the door to a wider range of applications with quantum dots in bioanalysis.

Bioanalytical applications make use of the unique optical properties of QDs enabled by size tuning. The effect of size tuning on optical properties is explained by a phenomenon called quantum confinement. As the particle gets smaller, the density of states near the band-edge decreases as the number of atoms decreases. Sufficiently small particle size results in a band gap in quantum dots with energy difference higher than kT, which prevents mobility of charge carrier from the valence band to the conduction band. [4] Once this limit is achieved, quantum confinement takes place. The smaller particles with less dense electronic states near the band-edge have a wider band gap than those that are larger in size, as illustrated in Figure 1.1. [2, 4]

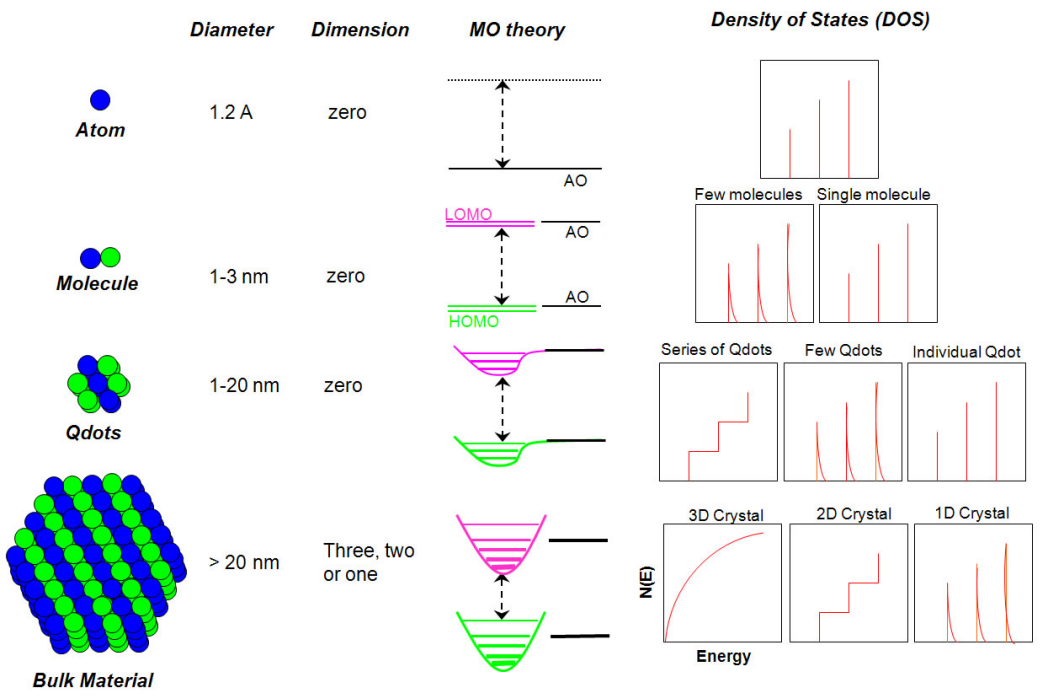

Figure 1.1 Illustration of the increasing density of states (DOS) with increases in the number of atoms in quantum dot particles. The density of states changes from discrete lines that correspond to energy gaps between clearly defined atomic orbitals (AO) with a single molecule to smoothed peak when a molecular orbital (MO) is comprised of numerous closely spaced AOs in 3D crystal. Size-tunable emission takes place when particle size is in the quantum dots (Qdots) regime. Energy gap refers to the energy difference between the highest occupied molecular orbital (HOMO) and lowest unoccupied molecular orbital (LUMO). Reproduced with permission from ref.[4] Copyright 2010 the authors.

A blue shift in emission corresponds to a higher band gap energy in smaller QDs, as illustrated in Figure 1.2.[2] Quantitatively, the limit where quantum confinement takes place is associated with the Bohr radius. The Bohr radius, r_B, defines the distance between an electron and a hole in semiconductor, approximated as eqn. 1.1, where m_e and m_h are the effective mass of electron and hole, respectively, and ħ, ε and e are the reduced Planck's constant, optical dielectric constant, and charge of an electron. When the radius of a particle is smaller than the Bohr radius, the effect of quantum confinement becomes non-negligible.[4]

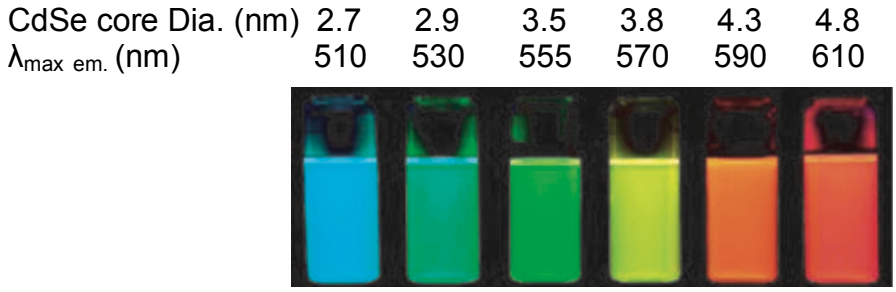

Figure 1.2 Photograph of differently sized QDs with size-tunable photoluminescence upon UV illumination. Image is adapted with permission from ref. [5]. Copyright 2005 Nature Publishing Group.

$$r_B = \frac{\hbar^2 \varepsilon}{e^2}\left(\frac{1}{m_e} + \frac{1}{m_h}\right) \tag{1.1}$$

II-VI semiconductors such as CdSe and CdTe, and III-V semiconductors such as InP, are popular materials for synthesis of QD cores. Although core-only materials provide size-tunable emission in QDs, another layer or multiple layers of inorganic semiconductor material called the shell(s) can be added for a few purposes. Depending on the materials used to grow the shell, the band-gap energy of the shell relative to the core serves different purposes. A type-I shell with conduction and valence band edges higher and lower, respectively, than that of the core is typically used to confine the exciton inside the core for enhanced quantum yield, as in the case of CdSe/ZnS core/shell QD.[3, 4] A type-II shell could be used to achieve localization of electron and/or hole in either the core or the shell. This approach offers a means to engineer QDs with band gap energy that is normally not feasible to achieve with the core material. For example, in near-infrared (NIR) emitting CdSe/CdTe/ZnSe QDs, a Type-II shell localizes an electron in the shell and the hole within the core to decrease the band gap energy.[3] Passivation of the core of QDs with a shell also serves to prevent leaching of QDs core material into the surrounding environment.

Tuning of the optical properties of QDs can also be achieved by alloying QDs. By incorporating materials with different optoelectronic properties, the optical properties of QDs can be tuned by the composition or percentage of the alloy, even while holding the

size of the QDs constant. Examples of alloyed QDs include $CdSe_xTe_{1-x}$, CdS_xSe_{1-x}, $CdxZn_{1-x}S$ and $Cd_{1-x}Zn_xSe$.[3] The advantages of alloying QDs include enhanced quantum yield through decreased surface defects, as well as narrow emission.[4]

1.1.2 Optical properties

Typically, QDs with core materials of CdSe have broad absorption spectra that span from the near-UV region to their first exciton peaks in the visible spectrum, with large molar absorption coefficients at their first exciton peak (10^4-10^6 $M^{-1}cm^{-1}$), and even higher magnitude absorption at shorter wavelengths. The high quantum yield of QDs (0.2-0.9) combined with its large and spectrally broad absorption leads to the superior brightness of QDs compared to conventional molecular fluorescent dyes. QDs have narrow, symmetric and tunable emission with a spectral full-width-at-half-maximum (FWHM) of 25-35 nm. These advantageous optical properties render QDs a favourable material for multiplexing, where excitation wavelengths are variable over a broad wavelength range, QDs with multiple emission colours can be spectrally well-separated due to their narrow emission FHWMs and all colours can be excited simultaneously.[2] Blinking, also known as fluorescence intermittency, is another unique optical property of QDs. Blinking occurs when the exciton is trapped at a surface state so that it takes a longer time scale (10^{-6} - 10^1 s) for it to return to the ground state. Though originated from imperfect surface, blinking has been utilized to observe single QDs for super-resolution imaging.[2]

1.1.3 Surface functionalization

Surface functionalization is a critical step toward the applications of QDs in bioanalysis. It involves first making QDs water-soluble, then customizing the QD surface for a particular application in bioanalysis through conjugation with biomolecules.

Since high-quality QDs from pyrolysis are dispersed in non-polar coordinating solvents, hydrophilic coatings needs to be applied to the QD surface for aqueous dispersion for biological applications. There are two types of coatings, which are defined based on the coating's anchoring scheme onto QDs: high affinity coordinating hydrophilic ligands (via

ligand exchange), and encapsulation of QDs with amphiphilic polymer. The synthesis of QDs often involves using TOPO (trioctylphosphine oxide) as surfactant, which consists of a phosphine oxide head group that coordinates to QDs and hydrophobic alkyl tails. Mass action with a large excess of thiol-containing hydrophilic ligands is frequently used to replace TOPO for making QDs water-soluble. Examples include mercaptoacetic acid (MAA), L-glutathione (GSH), and dihydrolipoic acid (DHLA).[6-8] Both MAA and GSH are monodentate ligands with one thiol functional group that coordinates to the Zn^{2+} ions in the ZnS shell of QDs, while DHLA is a bidentate ligand with two thiol groups for increased coating stability. Coatings of this sort work well at basic pH and low ionic strength, where the carboxylate group(s) is deprotonated and colloidal stability of QDs is driven by electrostatic repulsion between the negatively charged carboxylate groups. For coating stability in a wider range of pH and higher ionic strength with less nonspecific adsorption, DHLA ligand modified with polyethylene glycol (PEG) oligomers or zwitterionic functional groups were developed [9-11]. Though less popular, other coatings with polydentate ligands (e.g. oligomeric phosphines) for increased coating stability, and zwitterionic ligands (e.g. cysteine) for the purpose of decreasing hydrodynamic particle size and reducing non-specific adsorption have been developed.[12, 13] Ligands with other anchoring groups than thiols have also been developed. A dendron ligand with two carboxylate anchoring groups and eight terminal hydroxyl groups was found to enhance the luminescence and stability of CdSe/CdS core/ shell QDs compared to thiol-based dendron ligands.[14] Amphiphilic pegylated ligands with 4-substituted pyridine anchoring group was found to make CdSe QDs soluble in organic and aqueous solvents alike, with preserved luminescence.[15] Since the ligand exchange process involves removal of hydrophobic ligands on the QD surface, imperfect passivation of the QD could lead to a lower quantum yield after ligand exchange. The use of amphiphilic polymers resolves this problem because the amphiphilic polymers have pendant hydrophobic sidechains that interact with hydrophobic ligands to avoid their removal. [16, 17] The choice and design of coatings on QDs depend on the intended application, as coating largely determines colloidal stability at a chosen pH and ionic strength, hydrodynamic size, and nonspecific adsorption.

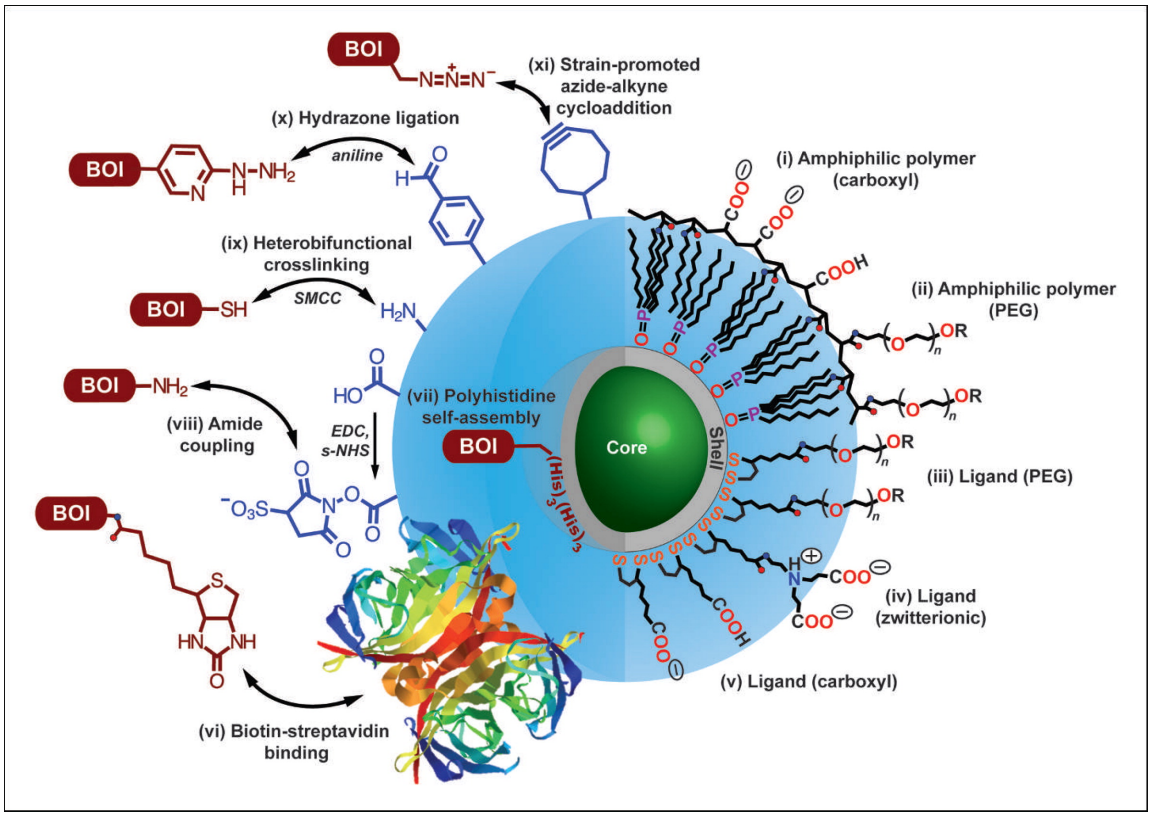

Figure 1.3 Diagram depicting different schemes of surface functionalization of QDs. Coatings for aqueous dispersion of QDs include amphiphilic polymers (i) with carboxyl(ate) groups or (ii) with PEG oligomers, bifunctional dithiol ligands (iii) with a distal PEG oligomer, (iv) with a distal zwitterionic functionality, (v) with a distal carboxyl(ate) group. Biomolecules of interest (BOI) could be conjugated to QD through (vi) biotin-streptavidin binding, (vii) polyhistidine self-assembly, (viii) amide coupling using EDC/s-NHS activation, (ix) heterobifunctional crosslinking using succinimidyl-4-(N-maleimidomethyl)cyclohexane-1-carboxylate (SMCC), (x) aniline-catalyzed hydrazone ligation, and (xi) strain-promoted azide–alkyne cycloaddition. Not drawn to scale. Image is reproduced with permission from Ref. [3]. Copyright 2013 Society for Applied Spectroscopy.

The conjugation of QDs with biomolecules is an essential step toward developing functional nanoparticles for a specific bioanalytical application. The attachment of biomolecules to QDs can be achieved through either covalent chemistries (Figure 1.3 (viii) – (xi)) or self-assembly (Figure 1.3 (vii)). The choice of bioconjugation chemistry is dependent on the application, the coating on QDs, and the biomolecule(s) of interest. In general, important considerations include control of conjugate valence, the biomolecular orientation, stability of the QD-bioconjugate, labeling efficiency in mild and aqueous conditions, as well as bioorthogonality.[2] Bioorthogonality is a criterion for specific

labeling, where the labeling chemistry does not react with other functional groups that are present in the biomolecules. An example of covalently bonded bioconjugation with high degree of bioorthogonality is the click chemistry between an alkyne and an azide.[18] Other bioconjugation methods based on covalent chemistry include the labeling of amine, carboxyl and thiol-reactive functional groups on the biomolecules via succinimidyl esters, carbodiimide coupling, and maleimides, respectively.[2] In self-assembly, the conjugation of biomolecules onto the QDs is through coordination or dative bonds. The labeling efficiency depends on the equilibrium dissociation constants as well as the concentration of nanoparticles and biomolecules. The stability of the assembly could be immensely improved by multidentate coordination, as in the example of polyhistidine coordination. The concept of polyhistidine-labeled proteins or peptides assembly onto QDs is based on the coordination of imidazole group in the amino acid histidine onto divalent metal ions, an idea long used in protein and peptide purification.[18] The presence of ZnS shell on QDs provides binding site of polyhistidine coordination for assembly of proteins and peptides.[19, 20]

1.1.4 Applications of QDs in bioanalysis

The advantageous optical and interfacial properties of QDs lend themselves to a variety of applications in biosensing. QDs are a potentially superior substitute for conventional organic fluorescent dyes. Their spectrally broad absorption with narrow and size-tunable emission offer tremendous advantages in multiplexed assays where a common excitation wavelength can be used for simultaneous excitation of multiple colours of QDs with well-resolved emission profiles. It has been demonstrated that emission from up to eight different colours of QD can be deconvoluted over the visible spectrum.[21] The brightness of QDs and their resistance to photobleaching allows spatial and temporal tracking and imaging of important cellular processes over a time period that would not be possible with conventional organic dyes.[22, 23]

QDs have also been used as donors or acceptors in energy transfer processes that are modulated through biorecognition events. In energy transfer processes such as

bioluminescence resonance energy transfer (BRET) and chemiluminescence resonance energy transfer (CRET), QDs serve as an optical acceptor for an excited state donor in close proximity that has been generated by a biological or chemical reaction. QDs also commonly serve as an energy donor to other proximal acceptors through Förster resonance energy transfer (FRET) upon photoexcitation.[3]

Theranostics is another intriguing application enabled by the unique optical properties and surface area of QDs, the latter used for delivery and release of drug cargo at target sites. As an example, a QD-RNA aptamer-doxorubicin conjugate was developed for prostate cancer cells recognition, therapeutic drug release, and imaging of these events enabled by FRET modulation in response to drug release. [21]

1.2 FRET and cFRET

Förster resonance energy transfer (FRET) is an energy transfer process that occurs between transition dipoles of an excited-state chromophore and a ground-state chromophore in close proximity through resonant dipolar interactions. The dependence of the FRET efficiency on the distance between the donor and the acceptor has enabled detection of target biomolecules through associative (e.g. binding) or dissociative (e.g. hydrolysis) activity, as well as by using FRET as a molecular ruler for sensing conformational changes in biomolecules induced by biological events. The unique optical properties of QDs make these materials very useful in FRET-based applications, which have been widely explored for biosensing.

1.2.1 Fluorescence

Fluorescence is an energy release process that involves the emission of a photon after a chromophore is photo-excited to a higher electronic state from its ground electronic state. After excitation, fluorescence is one of several possible pathways that an excited chromophore can use to relax to the ground electronic state. Other relaxation processes such as internal conversion, intersystem crossing and phosphorescence compete with fluorescence. Each of these processes occurs at different timescales. Figure 1.4 shows a

Jablonski diagram that illustrates the electronic states and transitions of a typical molecular chromophore.

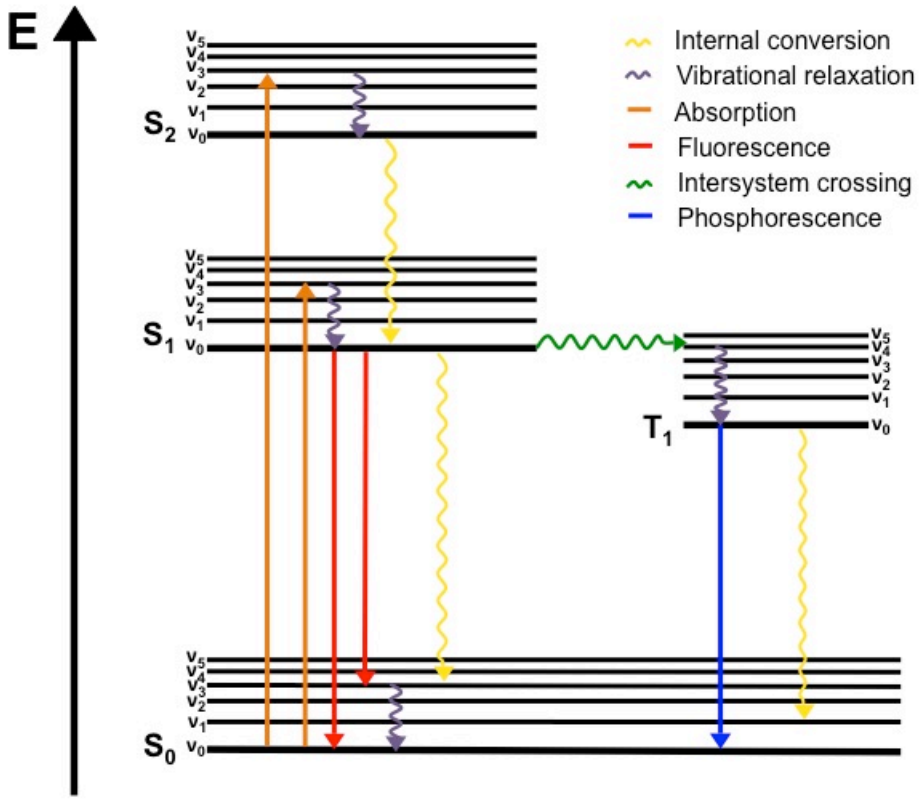

Figure 1.4 Jablonski diagram. S_0, S_1, S_2, and T_1 electronic states with superimposed vibrational levels from v_0 to v_5 shown. Rotational energy levels are within the vibrational levels and are not shown. Energy increases from bottom to top. Straight arrows specify electronic transitions that involve a photon. Wavy arrows specify transitions without a photon.

The electronic states in Figure 1.4 are arranged vertically with increasing energy from bottom to top, and horizontally with different spin multiplicity. S_0, S_1 and S_2 are the ground, fist excited and second excited singlet electronic states, respectively, and T_1 is the first excited triplet state. Each electronic state is associated with sub-levels that correspond to vibrational and rotational energy levels (not shown). Transitions that involve the absorption or emission of a photon are indicated as a straight arrow, and those without photons are indicated as wavy arrows. Photoexcitation occurs with photon absorption by a chromophore and is indicated in orange arrows. Photoexcitation promotes the chromophore from the lowest vibrational state of the ground electronic singlet state,

S_0 v_0, to higher vibrational states of the first, S_1 v_n, or second, S_2 v_n, excited singlet states. Once the photon is absorbed by the chromophore for excitation to a higher electronic state (a femtosecond process), a few processes may happen with different probabilities. Chromophores first undergo vibrational relaxation (purple wavy arrows) to release energy as heat by relaxing to lower vibrational modes of the same electronic state on the picosecond timescale.[24] For a chromophore in a higher electronic state, it may undergo internal conversion (yellow wavy arrows) to relax to a higher vibrational state of a lower excited electronic state with significantly overlapped vibrational probability functions. Since these processes happen much faster than fluorescence (nanosecond timescale), fluorescence almost always results from transitions from the lowest vibrational level of the first excited state to the ground electronic state.[24] If the excited chromophore has its spin multiplicity changed to a triplet state through intersystem crossing (green wavy arrow), phosphorescence could result (deep blue arrow), which is a forbidden transition and, therefore, has a relatively long excited triplet state lifetime of 10^{-4} to 10 s.[24] Due to the competition between different possible transitions, the efficiency for a chromophore to emit a fluorescence photon after photoexcitation is denoted by the quantum yield, Φ_f, which is a function of the rate constant of fluorescence, k_f, relative to the sum of k_f and the combined rate constant of all non-fluorescent relaxation processes mentioned above, k_{nr}, shown by eqn. 1.2. Another quantity that is often used to characterize a chromophore is the fluorescence lifetime, τ, which is the inverse of the sum of k_f and k_{nr}. Fluorescence lifetime is the time needed for excited chromophores to decay to 1/e of the initial intensity (~37%).

$$\Phi_f = \frac{k_f}{k_f + k_{nr}} \tag{1.2}$$

Although electronic states are discrete, the absorption and emission spectra of a typical chromophore consist of broad peaks. Thermal motions of the fluorophore and interactions with solvent cause broad absorption and emission bands that correspond to a group of allowed transitions between the vibrational and rotational levels of different electronic states. Since the spacing between vibrational levels is similar in both cases of ground and

first excited electronic states, and the same transition has similar probability for absorption and emission, a chromophore's absorption spectrum is approximately a mirror image of its fluorescence spectrum. Due to the fact that a chromophore emits a photon from the lowest vibrational level of the excited state to a higher vibrational state of the ground electronic state, energy loss through vibrational relaxation accompanying fluorescence leads to emitted photons having less energy than the absorbed photons, which is the reason for the Stokes shift between the absorption and emission spectra of a chromophore. A chromophore is photobleached when the repetitive absorption and emission processes cause an irreversible destructive effect on the chemical and electronic structure of the chromophore through reactions associated with the excited state, typically the excited triplet state with surrounding species.

1.2.2 FRET

Besides fluorescence, vibrational relaxation and other non-radiative relaxation pathways mentioned in the previous section, an excited chromophore may also relax to its ground electronic state by transferring its energy to a nearby chromophore through a resonant dipole-dipole interaction. This phenomenon is called Förster resonance energy transfer (FRET). The excited chromophore is called the FRET donor, and the ground-state chromophore in proximity to serve as the energy receiver is called the FRET acceptor, which could be either fluorescent or non-fluorescent. FRET is a widely used and powerful tool for bioanalysis and bioimaging due to the distance sensitivity of FRET efficiency at the length scale of biomacromolecules. The quenching efficiency of the donor (E) and FRET-sensitized photoluminescence (PL) ratio between the acceptor and the donor are two useful indicators in FRET-based analyses.

As one of the possible relaxation pathways for an excited-state donor, a FRET pathway competes with other relaxation pathways and the rate of FRET, k_{FRET}, is shown in eqn. 1.3, where κ^2 is the orientation factor, n is the refractive index of the medium, and N_A is Avogadro's number. Factors that affect k_{FRET} include the inverse decay rate of the donor ($1/\tau_D$), the quantum yield of the donor, Φ_D, the spectral overlap, J (λ), and distance

between donor and acceptor, r. As shown in eqn. 1.4, the spectral overlap depends on the normalized product of the wavelength-dependent emission intensity of the donor, $I_D(\lambda)$, and the wavelength-dependent molar absorption coefficient of the acceptor, $\varepsilon_A(\lambda)$, with λ being the wavelength. From eqn. 1.3, the Förster distance, R_0, (in units of centimeter) can be calculated through eqn. 1.5 with experimental measurements.

$$k_{FRET} = \frac{1}{\tau_D}\frac{9(\ln 10)\Phi_D \kappa^2 J(\lambda)}{128\pi^5 N_A n^4 r^6} = \frac{1}{\tau_D}\left(\frac{R_0}{r}\right)^6 = k_D \bullet \left(\frac{R_0}{r}\right)^6 \tag{1.3}$$

$$J(\lambda) = \frac{\int I_D(\lambda)\varepsilon_A(\lambda)\lambda^4 \, d\lambda}{\int I_D(\lambda) d\lambda} \tag{1.4}$$

$$R_0 = \sqrt[6]{(8.79\times 10^{-28} mol) n^{-4} \Phi_D \kappa^2 J} \tag{1.5}$$

Similar to the concept of quantum yield, the efficiency of FRET, E, is expressed as the rate of FRET relative to all relaxation pathways as shown in eqn. 1.6, where k_D is the sum of the rates of all other relaxation pathways except FRET, and $k_D = 1/\tau_D$. Substitution of k_{FRET} (eqn. 1.3) into eqn. 1.6 leads to the expression of FRET efficiency, E, in terms of Förster distance, R_0, and the donor-acceptor separation distance, r, in eqn. 1.6. It can be inferred from this expression that R_0 is the distance between donor and acceptor when the FRET efficiency is 50%. When $r = R_0$, the rate of FRET is same as the rate of all the other relaxation pathways.

$$E = \frac{k_{FRET}}{k_D + k_{FRET}} = \frac{R_0^6}{r^6 + R_0^6} \tag{1.6}$$

Since QDs are nanoparticles that are much larger than molecular fluorescent dyes, it was once questioned whether energy transfer between QD and an acceptor dye in proximity could be analyzed with the Förster dipole–dipole interaction mechanism. An experiment was done to test a QD-dye conjugate against Förster theory by measuring FRET efficiency (equivalent to quenching efficiency in this context) while varying the distance between QD and the acceptor dye. As shown in Figure 1.5, a good fit between experimental quenching efficiency and fitted data through Förster theory in eqn. 1.6 suggests that using a FRET model to study energy transfer with QDs is valid [25, 26].

Both experimental and fitted data in Figure 1.5 suggest that when the QD and acceptor dye are separated by a distance of R_0, quenching efficiency reaches 50% as predicted by Förster formalism in eqn. 1.6, and shown in the inset of Figure 1.5.

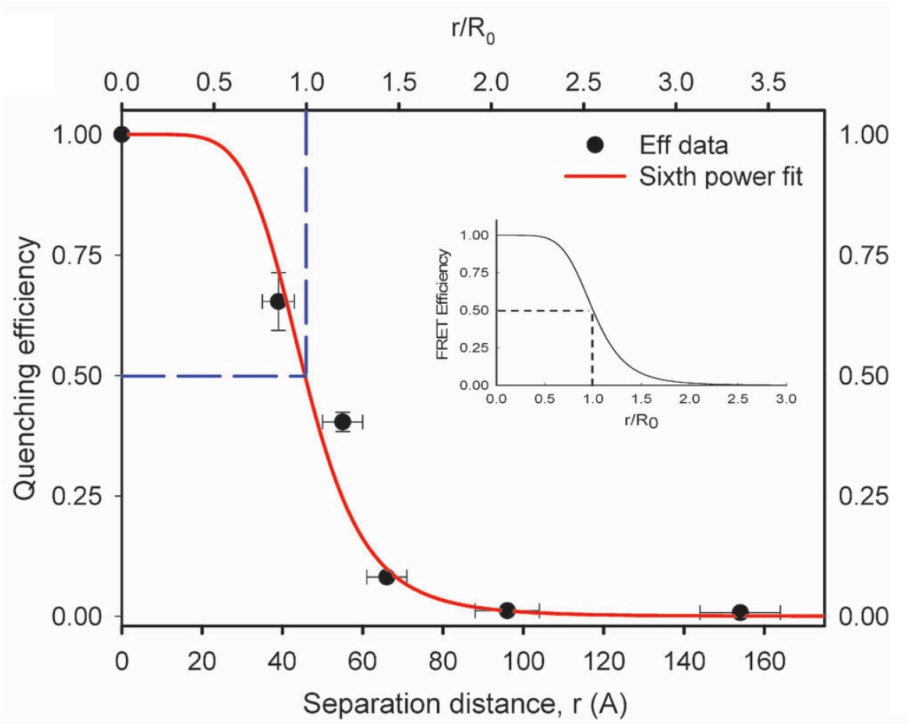

Figure 1.5 Comparison between experimental FRET efficiency data and fitted data through using Förster dipole–dipole formalism (eqn. 1.6). The inset shows the theoretical model of FRET Efficiency with respect to r/R_0. Note that quenching efficiency of donor reaches 50% when $r = R_0$. Figure is reproduced from ref. [25]. Reproduced by permission of the PCCP Owner Societies.

Since FRET decreases both the emission intensity and lifetime of the donor, its efficiency, E, can be calculated as shown in eqn. 1.7 from experimental data, I_D and I_{DA}, or τ_D and τ_{DA}, where I is an emission intensity and τ is a lifetime, the subscript $_D$ specifies the donor alone, and the subscript $_{DA}$ specifies the donor in the presence of acceptor. The photoluminescence (PL) ratio between the acceptor and the donor relates to the FRET efficiency through eqn. 1.8, where I_{AD} and I_{DA} are the emission intensity of the acceptor and donor, and Φ_A and Φ_D are the quantum yields of acceptor and donor. Substituting eqn. 1.6 into E in eqn. 1.8 yields the relationship between PL ratio and distance, r, in eqn. 1.8.

$$E = 1 - \left(\frac{I_{DA}}{I_D} \right) = 1 - \left(\frac{\tau_{DA}}{\tau_D} \right) \tag{1.7}$$

$$\text{PL}\, ratio = \frac{I_{AD}}{I_{DA}} = \frac{\Phi_A E}{\Phi_D (1 - E)} = \frac{\Phi_A}{\Phi_D} \left(\frac{R_0}{r} \right)^6 \tag{1.8}$$

In principle, QDs can act as a FRET donor or a FRET acceptor. FRET strategies that involve semiconductor QDs have been shown to obey the Förster dipole-dipole formalism.[27, 28] The spectrally broad and strong absorption of QDs renders it a preferred FRET donor rather than a FRET acceptor. As a FRET acceptor must be in its ground state, QDs with spectrally broad and strong absorption are prone to significant direct excitation that makes it inefficient as FRET acceptor.[29] As the FRET efficiency is inversely related to the distance between the donor and the acceptor as shown in eqn. 1.6, the size of QD core and its coatings could decrease FRET efficiency, that could otherwise be higher if a molecular dye is used. However, surface functionalization of QDs allows attachment of multiple acceptors, such as organic dyes, surrounding the QD as a central scaffold to increase the efficiency of energy transfer. [30] When multiple identical dye acceptors are equidistantly arrayed in proximity with the central QD as shown in the example in Figure 1.6, the rate of FRET, FRET efficiency, and PL ratio can be calculated as shown in eqns. 1.9, 1.10 and 1.11, where *a* is the number of identical acceptors surrounding the QD donor.

$$k_{FRET} = \frac{a}{\tau_D} \left(\frac{R_0}{r} \right)^6 \tag{1.9}$$

$$E = \frac{a k_{FRET}}{k_D + a k_{FRET}} = \frac{a R_0^6}{r^6 + a R_0^6} \tag{1.10}$$

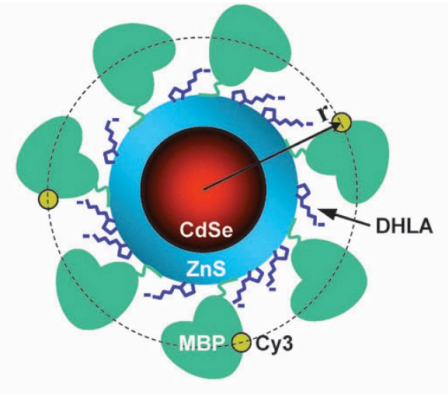

Figure 1.6 Schematic diagram of multiple copies of Cy3-labeled maltose binding proteins (MBP) assembled through hexahistidine self-assembly onto a central nanoscaffold of CdSe/ZnS QD. [31] Cy3-labeled MBPs are assembled equidistantly on an imaginary sphere with a fixed radius of *r* around the central QD. Radius of *r* that specifies the distance between centre of the QD core and acceptor dye in this diagram applies in eqn. 1.10.The image is reproduced with permission from ref. [25, 31]. Reproduced by permission of the PCCP.

$$\mathrm{PL}\,ratio = \frac{I_{AD}}{I_{DA}} = a\left(\frac{\Phi_A}{\Phi_D}\right)\left(\frac{R_0}{r}\right)^6 \tag{1.11}$$

1.2.3 Concentric FRET

When more than one type of acceptor dye is present on the surface of a QD donor, the phenomenon of concentric Förster resonance energy transfer (cFRET) is used to describe the modality where multiple competitive and sequential FRET pathways initiate at a central QD scaffold. Concentric FRET is distinguished from conventional FRET that involves only one type of acceptor by the presence of multiple energy transfer pathways. As illustrated in Figure 1.7, the presence of two acceptor dye species (yellow-emitting A555 and red-emitting A647) surrounding a green-emitting QD induces three energy transfer pathways. Upon excitation of the QD, energy can be transferred from the QD to the first acceptor dye A1 (A555 in Figure 1.7), and subsequently from A1 to the second acceptor dye A2 (A647 in Figure 1.7). Although there is more significant spectral overlap between QD and A1 than between QD and A2, the competitive pathway from QD to A2 is not negligible. Consistent with the prediction from first principles, the quenching

efficiency of the QD, Q_{QD}, is expressed as eqn. 1.12, where k_{QD} is the equivalent of k_D in eqn. 1.6, $k_{QD\text{-}A1}$ and $k_{QD\text{-}A2}$ are the FRET rates of pathways from QD to A1 and from QD to A2, and M and N are the number of A1 and A2 on the surface of sphere concentric to the QD.[32]

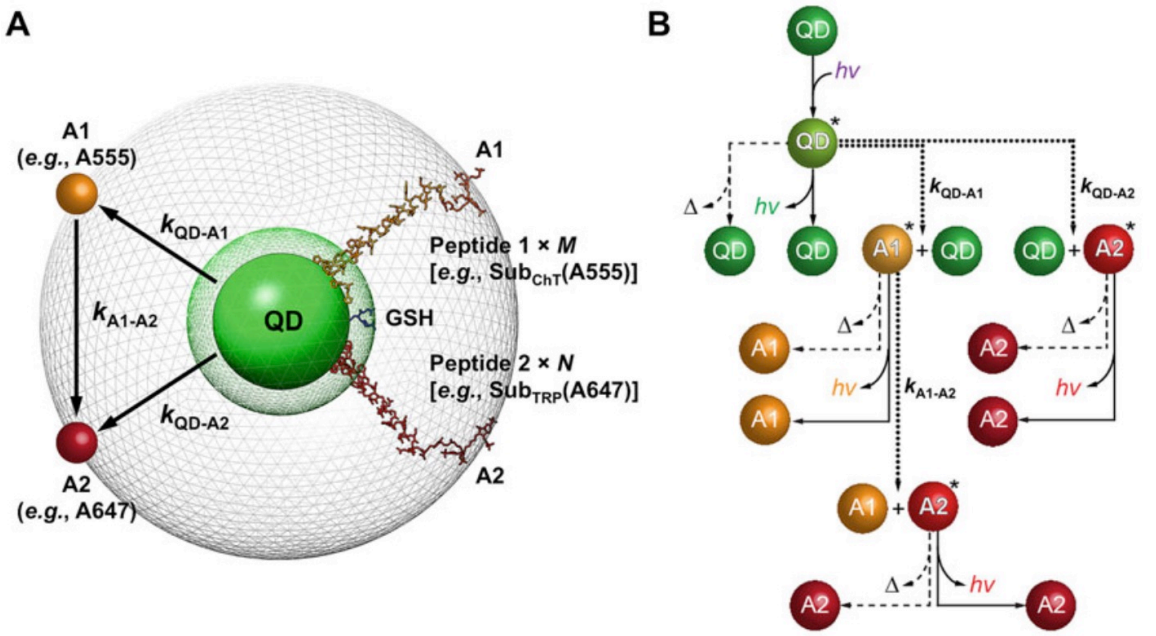

Figure 1.7 cFRET. (A) Simplified schematic diagram of a QD–$(A1)_M$–$(A2)_N$ cFRET configuration assembled with A555 and A647-labeled peptide substrates for chymotrypsin and trypsin. The right half the figure shows the assembly of the cFRET configuration that consists of the green-emitting QD with hydrophilic glutathione (GSH) ligand coating, and A1- and A2-labeled peptides self-assembled to the QD through polyhistidine tags. The left half of the figure shows the three energy transfer pathways associated with FRET rates, $k_{QD\text{-}A1}$, $k_{QD\text{-}A2}$, and $k_{A1\text{-}A2}$ within the cFRET configuration. (B) Flow chart showing all possible energy transfer and relaxation pathways in a cFRET configuration after initial photoexcitation of the QD. The asterisk denotes an excited chromophore, *hv* is a photon, and Δ represents heat. The image in (A) is reproduced with permission from ref [32]. Copyright 2015 American Chemical Society. The image in (B) is reproduced with permission from ref. [33]. Copyright 2017 Springer Science+Business Media New York**.**

$$Q_{QD} = 1 - \left(\frac{I_{QD-A1-A2}}{I_{QD}} \right) = \frac{M k_{QD}^{-1} k_{QD-A1} + N k_{QD}^{-1} k_{QD-A2}}{1 + M k_{QD}^{-1} k_{QD-A1} + N k_{QD}^{-1} k_{QD-A2}} \qquad (1.12)$$

The FRET efficiencies of each of the three pathways were experimentally tested against mathematic models indicated in eqns. 1.13, 1.14 and 1.15.[32]

$$E_{QD-A1} = \frac{Mk_{QD}^{-1}k_{QD-A1}}{1 + Mk_{QD}^{-1}k_{QD-A1} + Nk_{QD}^{-1}k_{QD-A2}} \tag{1.13}$$

$$E_{QD-A2} = \frac{Nk_{QD}^{-1}k_{QD-A2}}{1 + Mk_{QD}^{-1}k_{QD-A1} + Nk_{QD}^{-1}k_{QD-A2}} \tag{1.14}$$

$$E_{A1-A2} = \frac{Nk_{A1}^{-1}k_{A1-A2}}{1 + Nk_{A1}^{-1}k_{A1-A2}} \tag{1.15}$$

Similar to the concept of equidistant model presented in Figure 1.6, the validity of eqns. 1.12-1.14 is based on acceptor dyes occupying a sphere with fixed radius central to the QD as shown in Figure 1.8.

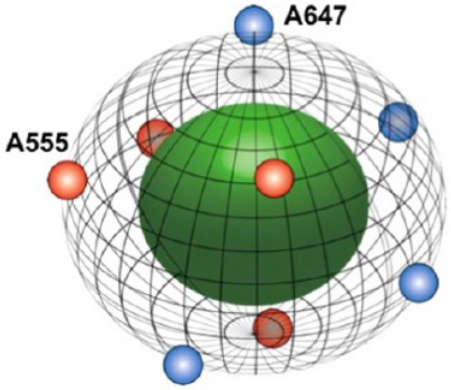

Figure 1.8 Schematic illustration of distribution of four A555 and four A647 on an imaginary sphere central to a QD in a cFRET configuration. In the equidistant model, both the distribution of A555 and A647 is radially symmetric to the QD, and the distance between A555 and A647 is maximized. Image is reproduced with permission from ref.[34]. Copyright 2012 American Chemical Society.

Eqn. 1.15 shows the expression for the FRET efficiency of the A1-A2 pathway predicted as if there is only one type of dye acceptor (A2) separated with a fixed distance to the donor (A1). In a concentric FRET model, this condition is not strictly fulfilled as illustrated in Figure 1.9, where a distribution of varying distances could be drawn from each A2 (A647) to an excited A1 (A555) in a cFRET configuration. In spite of this, experimental data tested against eqn. 1.15 suggests the varying distribution of A2 (A647) relative to A1 (A555) could be reduced to a single average distance.[32]

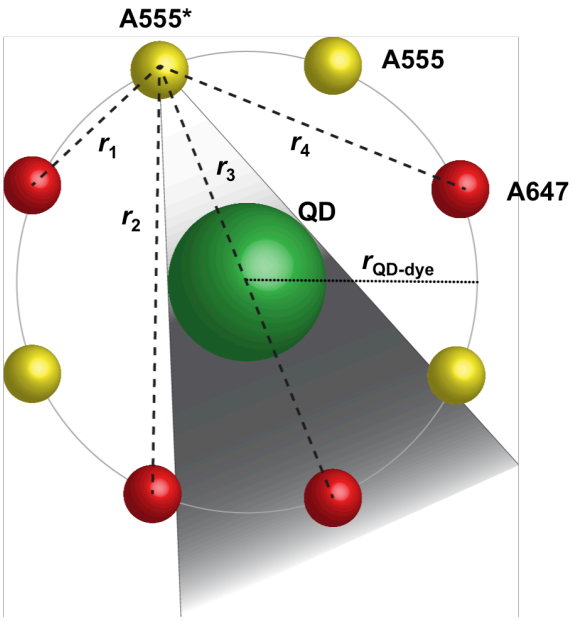

Figure 1.9 Schematic diagram depicting positions of A555 and A647 on the imaginary surface sphere of QD in a cFRET configuration. Radial symmetry persists in QD–A555 and QD–A647 donor-acceptor FRET pairs. A555–A647 FRET pair lacks radial symmetry, and various distances, from r_1 to r_4, could be drawn between an excited A555 and various A647. Image is reproduced with permission from ref. [32] Copyright 2015 American Chemical Society.

PL emission ratios between each of the acceptor dyes and the QD are more useful parameters than FRET efficiency in bioanalytical applications. The PL ratios depend on two quantities, the PL intensity of the dye and PL intensity of the QD, that change in opposite direction when FRET occurs. Hence, PL ratios are more sensitive parameters than FRET efficiency, which is related only to the quenching of QD PL. Moreover, the use of PL ratios allows cFRET events to be tracked with more than one parameter, instead of only FRET efficiency. This is especially important in cFRET-based analysis, where two PL ratios can be simultaneously used to track the number of both types of acceptor dyes on the QD, and a particular set of PL ratios describes a unique combination of M and N, whereas various combinations of M and N may lead to the same FRET efficiency. PL ratios are related to the quantum yields of the emitter and the efficiency of the related FRET-sensitized pathways, and can be expressed as eqns. 1.16 and 1.17, and further expanded with substitutions of eqns. 1.13, 1.14 and 1.15.[32]

$$\frac{I_{A1}}{I_{QD}} = \left(\frac{\Phi_{A1}}{\Phi_{QD}}\right)\frac{E_{QD-A1}(1-E_{A1-A2})}{1-E_{QD-A1}-E_{QD-A2}} = \left(\frac{\Phi_{A1}}{\Phi_{QD}}\right) M k_{QD}^{-1} k_{QD-A1}\left(\frac{1}{1+N k_{A1}^{-1} k_{A1-A2}}\right) \tag{1.16}$$

$$\frac{I_{A2}}{I_{QD}} = \left(\frac{\Phi_{A2}}{\Phi_{QD}}\right)\frac{E_{QD-A2}+E_{QD-A1}E_{A1-A2}}{1-E_{QD-A1}-E_{QD-A2}} = \left(\frac{\Phi_{A2}}{\Phi_{QD}}\right)\left[N k_{QD}^{-1} k_{QD-A2} + M k_{QD}^{-1} k_{QD-A1}\left(\frac{N k_{A1}^{-1} k_{A1-A2}}{1+N k_{A1}^{-1} k_{A1-A2}}\right)\right] \tag{1.17}$$

1.3 FRET-based QD nanosensors

1.3.1 FRET-based DNA assays with QDs

Detection and quantification of oligonucleotides are important in hereditary and infectious disease detection, as well as forensic and paternity analysis. Detecting DNA sequences faces the challenge of lowering detection limits, increasing sensitivity and specificity, as well as reducing the number of steps during analysis. As an important preliminary step in detecting DNA sequences in conventional methods, the polymerase chain reaction (PCR) established in 1985 is a well-known technique for amplification of DNA. This technique relies on the enzymatic amplification of the target DNA by using DNA polymerase mediated by a primer.[35] PCR-based DNA detection requires either control from professional analysts, or an automated system that carries through the reaction conditions required by PCR, making it not ideal for point-of-care diagnostic device or certain applications such as cellular detection of DNA/RNA. Aiming at quick and simple diagnostic techniques, a great number of recently developed DNA assays combined sequence recognition and signal transduction by utilizing, for example, allosteric enzyme, oligonucleotides-bound gold nanoparticles with silver reduction, magnetically-induced electrochemical DNA sensor and immobilized molecular beacon [36-39]

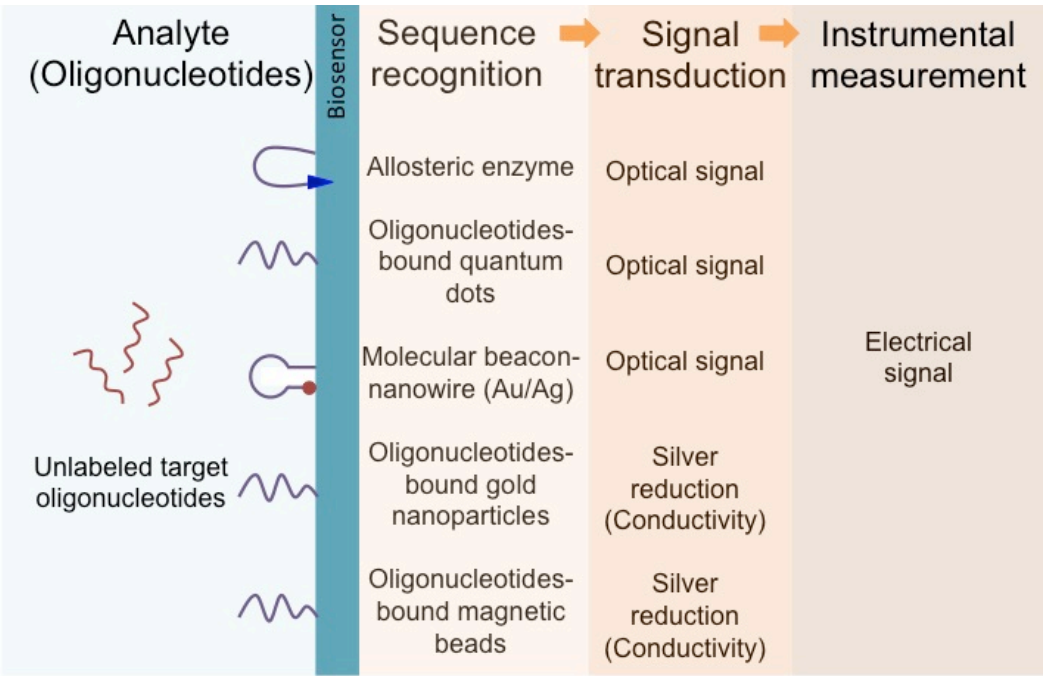

Figure 1.10 Diagram illustrating detection schemes of biosensor that unites both sequence recognition and signal transduction.

Owing to their unique optical and surface functionalization properties, QDs have been widely explored for the detection of nucleic acids. In assays with QDs, oligonucleotides serve as the target with sequence complementarity for recognition, as well as an entity that brings a dye acceptor in close proximity with the QD for signal transduction. As one of the examples shown in Figure 1.11, QDs in combination with FRET have been explored for detection of virus DNA fragments and DNA polymerase.[40-42] An attempt for multiplexed detection shown in Figure 1.12, two DNA fragments were detected at nanomolar concentrations using two QDs that act as the energy donor for two separate FRET channels, one with green emission and the other with red emission.[43] Later, multiplexed detection of DNA fragments was achieved through using only one QD, with two separate FRET channels that involve two acceptor dyes, or one acceptor dye with another individual dye reporter.[44, 45] The latter work utilized the surface functionality of QD for becoming a nanoconcentrator that bundles two emission channels on one central scaffold for single-molecule detection.

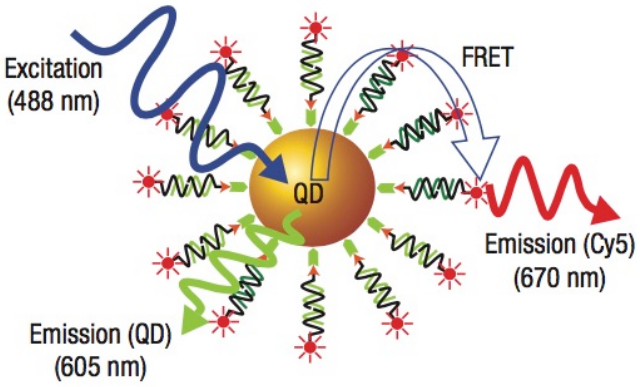

Figure 1.11 Schematic diagram of a FRET-based quantum dot biosensor for oligonucleotides detection. Target DNA (green strands) bring Cy5-labeled reporter probe in proximity with the quantum dot (QD) through hybridization with capture probe. FRET-sensitized emission from Cy5 upon photo-excitation of the QD signals detection of target strands. Image is reproduced with permission from ref. [42] Copyright 2005 Nature Publishing Group.

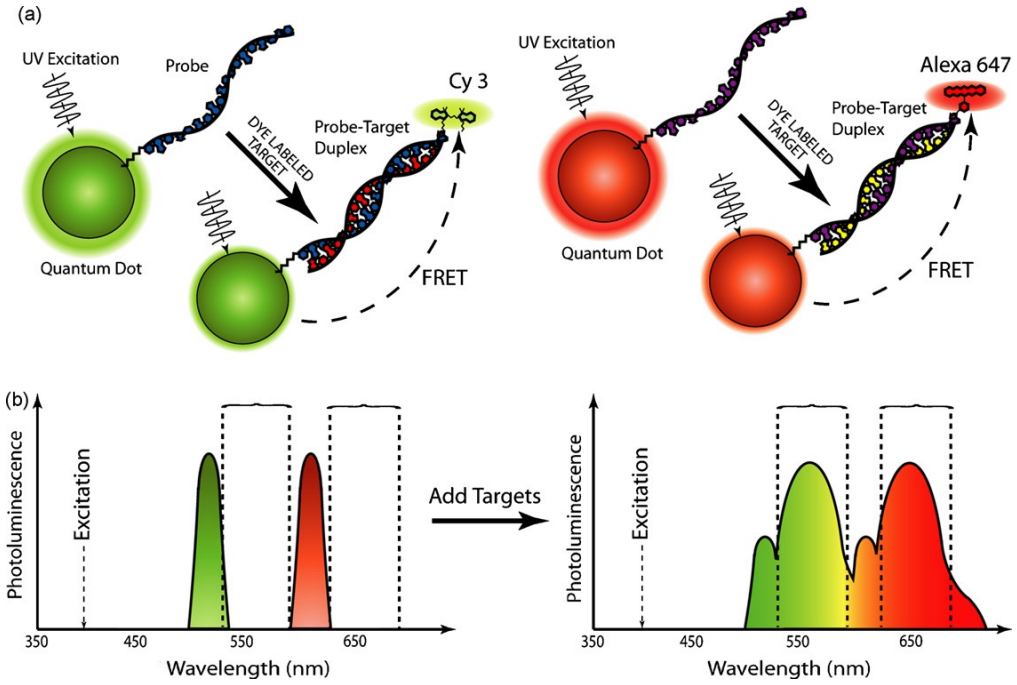

Figure 1.12 Schematic diagram of multiplexed detection of two target strands through two quantum dots FRET-based channels. (A) FRET-sensitized emission from Cy3 and Alexa Fluor 647 upon hybridization between the dye-labeled targets and their respective QD-Probe. (B) The two separate FRET channels are resolved on visible spectrum, with one emitting in the green region and the other in the red. Image is reproduced with permission from ref.[43] Copyright 2006 Elsevier B.V.

1.3.2 cFRET-based QD assays

Concentric FRET-based nanosensors enabled by the optical and interfacial properties of QDs have been shown to have promising applications in bioanalysis. The ability to co-assemble multiple copies of different types of chromophores onto the QD allows interrogation of multiple energy pathways that could be employed for quantitation. A well-studied cFRET configuration with QDs was constructed with the use of a central green-emitting QD, yellow-emitting Alexa Fluor 555 (A555) (or Cy3 as a substitute) and red-emitting Alexa Fluor 647 (A647) dyes.[34, 46] Simultaneous quantitative analysis of two bioanalytical parameters was enabled through the two distinguished yet functionally related emission channels built around the central QD. For example, the cFRET configuration of QD–A555–A647 was designed for the study of interfacial arrangement of assembled bioconjugates on the surface of the QD, and used for simultaneous detection of enzymatic activities of trypsin and chymotrypsin as illustrated in Figure 1.13.[34] Furthermore, a similar green cFRET configuration QD524–Cy3–A647 was demonstrated for simultaneous detection of proteolytic concentration and activity as illustrated in Figure 1.14, through the use of dye-labeled peptide substrates and dye-labeled aptamers assembled to the QD.[46] The green cFRET configuration has been characterized in terms of PL intensities and PL decays for its validation against conventional formalism for better understanding of photophysics behind this cFRET configuration, and its susceptibility for photobleaching under fluorescence microscope imaging.[32]. A cFRET-based fluorescence microscopic imaging experiment has also been demonstrated for imaging and tracking of two protease activities in a capillary tube with spatiotemporal resolution shown in Figure 1.15.[47]

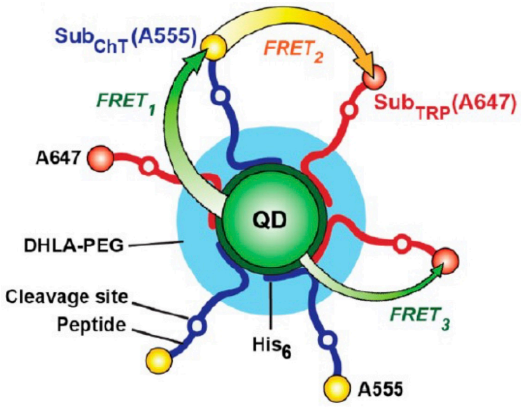

Figure 1.13 An illustration of green QD–A555–A647 cFRET configuration constructed for simultaneous detection of protease activities of trypsin (TRP) and chymotrypsin (ChT). Central poly(ethylene glycol)-appended dihydrolipoic acid (DHLA-PEG) coated green-emitting QD was bioconjugated with A555-labeled peptide substrates of (Sub) chymotrypsin and A647-labeled peptide substrates of trypsin through hexahisitidine (His_6) assembly. Image is reproduced with permission from ref. [34] Copyright 2012 American Chemical Society.

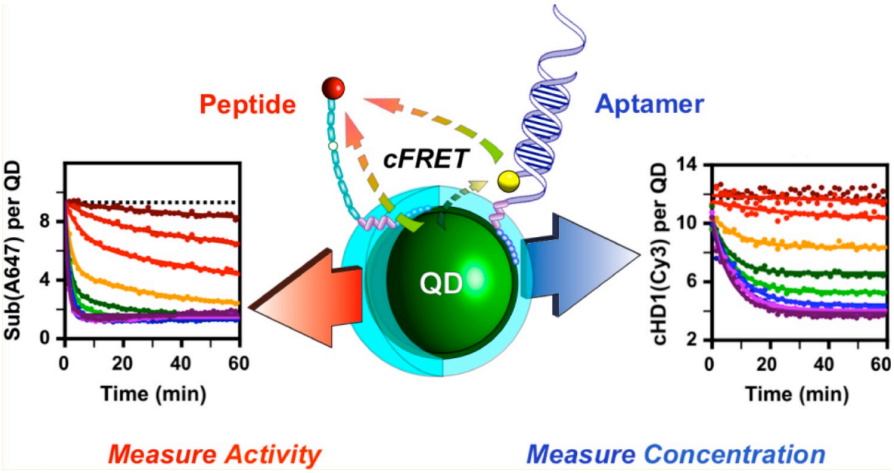

Figure 1.14 An example of cFRET-based quantum dots biosensor for simultaneous detection of protease activity and concentration. A green-emitting QD524 is used as energy donor to yellow-emitting Cy3 and red-emitting A647 for assembly of a cFRET configuration. Protease concentration is tracked through the Cy3 channel with aptamer, and protease activity is tracked through A647-labeled peptide. Image is reproduced with permission from ref. [46] Copyright 2014 American Chemical Society.

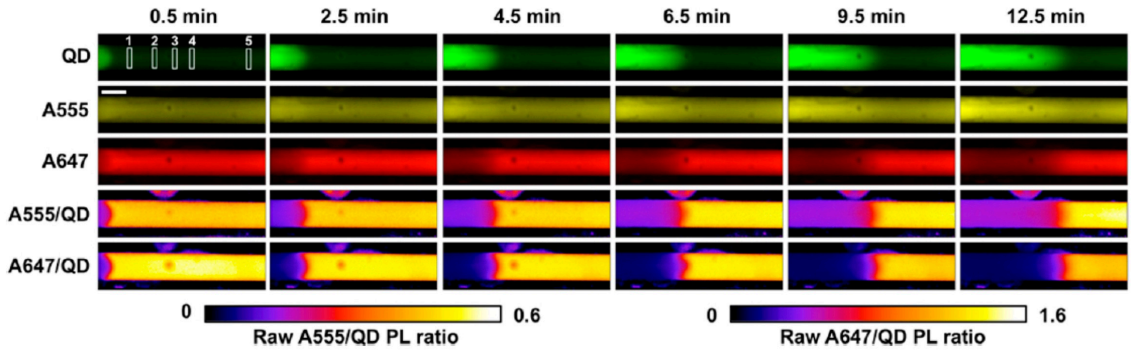

Figure 1.15 False-color images of QD, A555, and A647 PL intensity within the capillary, and raw A555/QD and A647/QD PL ratio images (not corrected for crosstalk and background), at different time points after adding mixture of trypsin and chymotrypsin. The scale bar is 400 μm. Trypsin and chymotrypsin were added to the left end of the capillary tube filled with solution of cFRET probe containing $[Sub_{ChT}(A555)]_M$–QD–$[Sub_{TRP}(A647)]_N$. PL intensity of QD increases from left to right as time goes because of recovery of QD PL upon digestion of $Sub_{ChT}(A555)$ and $Sub_{TRP}(A647)$. All of PL intensity of A647, raw A555/QD PL ratio and raw A647/QD PL ratio decrease due to loss of FRET upon enzymatic cleavage of dye-labeled substrates by both enzymes. PL intensity of A555 shows no apparent decrease due to crosstalk from QD. Image is reproduced with permission from ref. [47] Copyright 2015 American Chemical Society.

1.4 Contributions of this thesis

The interesting properties of QDs have made these materials popular for biological sensing. The role of the QD in cFRET configurations takes full advantage of its interfacial and superior optical properties. Previously reported cFRET-based applications with QDs only adopted green-emitting QDs for assembly of peptide-linked configurations. Work in this thesis takes the studies of cFRET to the next important stage, where a red-shifted configuration is shown to be equally functional as the conventional green-emitting configuration, with improvements in certain aspects, and an oligonucleotide-linked configuration is demonstrated for potential expansion of cFRET applications. It is important to design and characterize a cFRET configuration with red-shifted emission channels to not only demonstrate that the cFRET configuration could be expanded to other QD-dyes combinations, but also to seek potential improvements on qualities of biosensing in terms of detection limit, sensitivity, compatibility in biological media, and susceptibility for photobleaching conditions. Moreover, demonstration of an oligonucleotide-linked cFRET configuration for multiplexed detection of two

oligonucleotide fragments in this thesis expands cFRET to a wider range of applications in bioanalysis.

In Chapter 2, the bottom-up experimental design of a long-wavelength cFRET configuration is introduced with details on synthesis, assembly and purification. Important results on characterization of the long-wavelength cFRET configuration and its application in an oligonucleotide-linked modality is presented and discussed in Chapter 3. Validation of the long-wavelength cFRET configuration against conventional FRET theories as well as energy transfer pathways in conventional cFRET model was done through rate analysis and studies of FRET efficiencies. Photophysical properties of the cFRET configuration were analyzed and compared with the prototypical green cFRET configuration to reveal both weaknesses and advantages. Furthermore, application of the new long-wavelength cFRET configuration to oligonucleotide-linked modality for quantification confirms that the cFRET strategy is not limited to peptide-related systems. Overall, this work supports that QD-based cFRET strategy is an advantageous bioanalytical tool that could be generalized to other QD-dyes combinations for a wide range of applications.

Chapter 2
Experimental methods

2.1 Materials

CdSe/CdS/ZnS core/shell/shell QDs with peak photoluminescence at ~605 nm (QD605) and CdSe/CdS/ZnS QD520 were synthesized by a collaborator using previously described methods. [49, 50] Alloyed CdSeS/ZnS QD525 were from Cytodiagnostics (Burlington, ON, Canada). QDs are named after the wavelength of peak photoluminescence. Hydrophobic QDs were coated with glutathione (GSH) ligands for aqueous dispersion via a ligand exchange procedure described in Section 2.2. Alexa Fluor 633 C5 maleimide and Alexa Fluor 680 C2 maleimide were from Thermo-Fisher Scientific (Carlsbad, CA, USA). Synthetic peptides were from Bio-Synthesis Inc. (Lewisville, TX, USA) and synthetic oligonucleotides were from Integrated DNA Technologies (Coralville, IA, USA). The peptide and oligonucleotide sequences are shown in Table 2.1 and Table 2.2, respectively. Phosphate buffered saline (PBS), triethylammonium acetate (TEAA) buffer, borate buffer, tris-borate buffer were sterilized by either filtration through a 0.22 μm filter or autoclaving. All other reagents were from Sigma-Aldrich (Mississauga, ON, Canada).

Table 2.1 Dye-labeled peptide sequences and modifications

Name	Sequence[a]
Pep(A633)	Ace-HHHHHHSPPPPPPSGQGEGGNSDDDDKSGNGC-A633
Pep(A680)	Ace-HHHHHHSPPPPPPSGQGEGGNSDDDDKSGNGC-A680

[a] Peptide sequences (amino acids) are indicated with uppercase letters and written from N-terminal to C-terminal (Ace = *N*-acetylation). Adapted from ref.[48] by permission of The Royal Society of Chemistry. Copyright 2016.

Table 2.2 Oligonucleotide sequences and modifications

Name	Sequence[a]
Probe 1	DTL-5′atc tct tgg ccg tgt gga t-3′
Block (Blk) 1(A633)	5′- cac ggc caa gag at-3′-(A633)
Target (Tgt) 1	5′-atc caca cg gcc aag aga t-3′
Probe 2	DTL-5′-gct gtg tga gag acg gga aa-3′
Block (Blk) 2 (A680)	5′-cgt ctc tca cac agc -3′-(A680)
Target (Tgt) 2	5′-ttt ccc gtc tct cac aca gc-3′

[a] Oligonucleotide sequences (nucleotides) are indicated with lowercase letters (DTL = dithiol linker; see Section 2.4 for details). Adapted from ref.[48] by permission of The Royal Society of Chemistry. Copyright 2016.

2.2 Glutathione ligand exchange on QDs

QD605 (25 μL, ~200 μM) in toluene were diluted with 900 μL of chloroform. A solution of glutathione (GSH) dissolved in methanolic tetramethylammonium hydroxide (TMAH; 300 μL, ~1 M GSH, 25% w/w TMAH) was then added. This mixture was vortexed and let stand at room temperature for 24 h. Borate buffer (200 μL; 50 mM, pH 9.5, 250 mM NaCl) was added. The mixture was vortexed then let phase separate to extract GSH-coated QDs into the aqueous phase. The organic layer was discarded, and the GSH-QDs were separated from excess GSH by precipitation: a volume of ~800 μL of ethanol was added, and the QDs were then centrifuged at ~5500 rcf for 4 min. The supernatant was discarded and the precipitated QDs were redispersed in 200 μL borate buffer (50 mM, pH 9.5, 250 mM NaCl). Three additional rounds of ethanol precipitation were repeated before final redispersion of the purified GSH-coated QDs in borate buffer (50mM, pH 8.5) at a concentration of ~30 μM.

2.3 Peptide labeling

Peptide (~0.25 mg, ~75 nmol) was dissolved in 5 μL of 50% v/v MeCN (aq) and mixed with either (i) 8 μL of thiol-reactive Alexa Fluor 680 C2 maleimide (11.1 mg mL^{-1}, ~90 nmol; Thermo-Fisher Scientific, Carlsbad, CA, USA) or (ii) 13 μL of thiol-reactive Alexa Fluor 633 C5 maleimide (11.1 mg mL^{-1}, ~111 nmol; Thermo-Fisher), both of which were dissolved in DMF. The reaction mixture was diluted to 100 μL with phosphate buffered saline (PBS; 10 mM, pH 7.0, 50 mM NaCl), vortexed, and agitated for 24 h at room temperature while protected from light. To purify the dye-labeled peptide from excess dye, the reaction mixture was loaded into a cartridge filled with Ni^{2+}-nitrilotriacetic acid (NTA)-agarose. The Ni^{2+}-NTA- agarose with bound peptide was washed with 2 × 10 mL of PBS, 10 mL of PBS with 50% v/v ethanol, and another 2 × 10 mL of PBS. The dye-labeled peptide was then eluted from Ni^{2+}-NTA using 3 × 0.5 mL portions of imidazole solution (300 mM in PBS; filtered through activated charcoal prior to use). The dye-labeled peptide in the imidazole eluate was then transferred to a cartridge filled with Amberchrom CG300M resin for desalting. After binding the dye-labeled peptide, the resin was washed with 4 × 10 mL of triethylammonium acetate (TEAA) buffer (0.2 M, pH 7.0) and subsequently eluted with 1 mL of 70% v/v MeCN (*aq*). The amount of dye labeled peptide was quantified by UV-visible spectrophotometry, split into 10 nmol fractions, each fraction concentrated to dryness under vacuum and stored at –20 °C until needed.

2.4 Dithiol-terminated linker (DTL) synthesis

A succinimidyl ester-activated dithiol-terminated linker (DTL; protected as a disulfide) was synthesized as summarized in Figure 2.1, which is based on a published procedure with minor modifications as described below.[51]

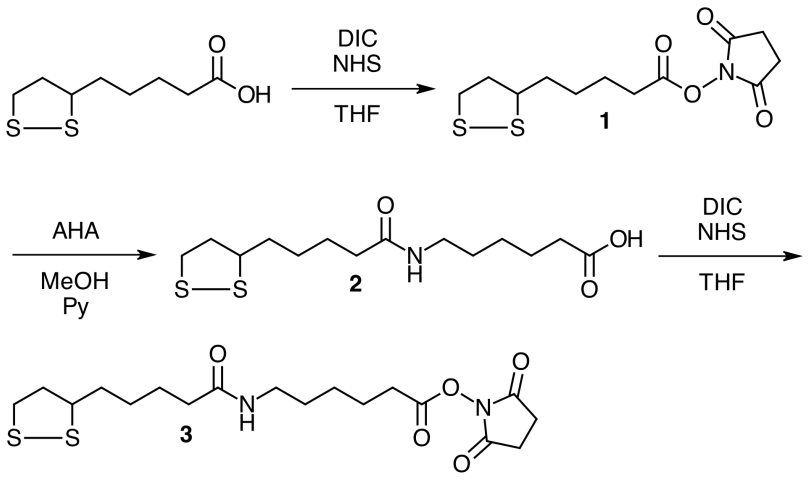

Figure 2.1 Synthesis of dithiol-terminated linker (DTL). Reproduced from ref.[48] by permission of The Royal Society of Chemistry. Copyright 2016.

Synthesis of compound **1**

Lipoic acid (2.0 g, 9.7 mmol) and *N*-hydroxysuccinimide (NHS; 1.38 g, 12 mmol) were dissolved in 60 mL of tetrahydrofuran (THF). *N,N*′-Diisopropylcarbodiimide (DIC; 1.9 mL, 12 mmol) was added to 5 mL of THF and this solution was added dropwise to the solution of lipoic acid and NHS. The reaction was stirred for 5–6 h at room temperature and the resulting white precipitate was filtered by gravity. The filtrate was collected and concentrated to ~3 mL using a rotary evaporator before isopropanol was added and the mixture left at –20 °C overnight to crystallize **1**. The pale yellow crystals were collected by vacuum filtration, washed with ether, and dried. The product **1** (1.7 g, 5.6 mmol, 58% yield) was stored at –20 °C until needed.

Synthesis of compound **2**

Compound **1** (0.60 g, 2.0 mmol) and 6-aminohexanoic acid (AHA; 0.50 g, 3.8 mmol) were added to a solution of 20 mL of anhydrous methanol (MeOH) mixed with 10 mL of pyridine (Py; dried over Na_2SO_4). The reaction mixture was then stirred overnight at room temperature. The product was extracted into dichloromethane (DCM; 50 mL) against an acidic aqueous phase (300–350 mL, 1–3 M HCl, 0.4–0.6 M NaCl). The organic phase was collected and washed three times with an acidic aqueous phase, then

dried over sodium sulfate. The washed DCM layer was concentrated in a rotary evaporator until ~5 mL DCM remained, at which point 20 mL of diethyl ether was added. These concentration and dilution with ether steps were repeated three times to obtain solvent that was ~99% ether. The ether was then quickly evaporated to dryness under reduced pressure to obtain a pale yellow solid **2** (0.30 g, 0.94 mmol, 47% yield) that was stored at –20 °C until needed. ESI^+ MS (MeOH): calc. for $C_{14}H_{25}NO_3S_2$ $[M+H]^+$ *m/z* = 320.5, found *m/z* = 320.1 (Figure 2.2A). ESI^- MS (MeOH): calc. for $C_{14}H_{25}NO_3S_2$ M^- *m/z* = 318.5, found *m/z* = 318.0 (Figure 2.2B).

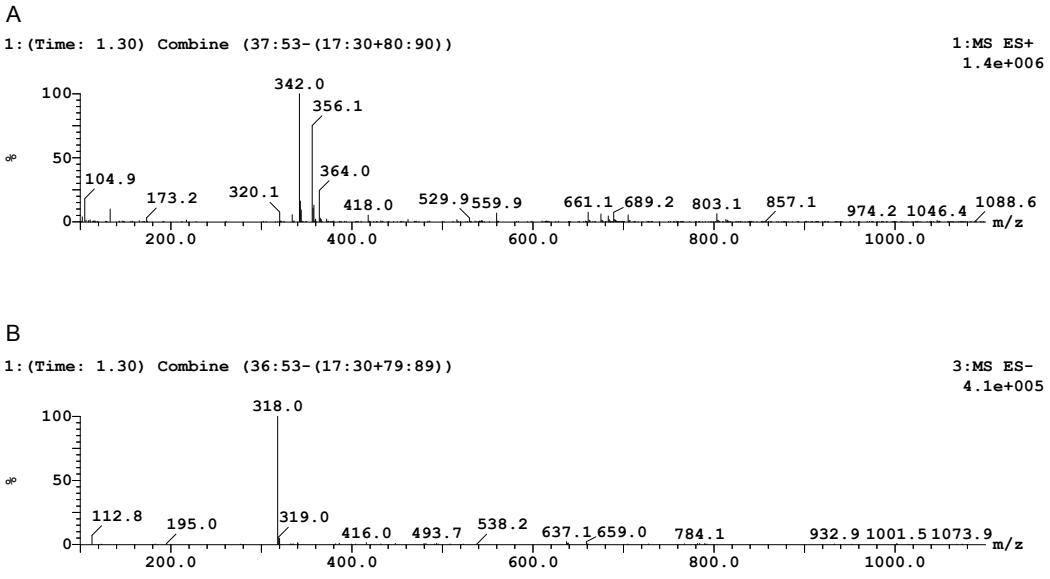

Figure 2.2 ESI-MS spectra of compound 2. (A) The $[M+H]^+$ peak is seen at m/z 320.1 in positive ion mode. Peak at m/z 342.0 corresponds to the sodium adduct of compound 2. (B) Negative ion mode spectrum showing the M^- peak for compound **2** at m/z 318.0, corresponding to the loss of a proton.

Synthesis of compound **3**

Compound **2** (0.10 g, 0.31 mmol) was dissolved in THF with 1.2 equiv. of DIC and NHS. The synthesis of **3** was then done following the same procedure as the synthesis of compound **1**. The crystallized product **3** (0.080 g, 61% yield) was stored at –20 °C until needed. ESI^+ MS (MeOH): calc. for $C_{18}H_{28}N_2O_5S_2$ $[M+H]^+$ *m/z* = 417.6, found *m/z* =

417.0 (Figure 2.3A). ESI⁻ MS (MeOH): calc. for $C_{18}H_{28}N_2O_5S_2$ M^- *m/z* = 415.6, found *m/z* = 414.9 (Figure 2.3B).

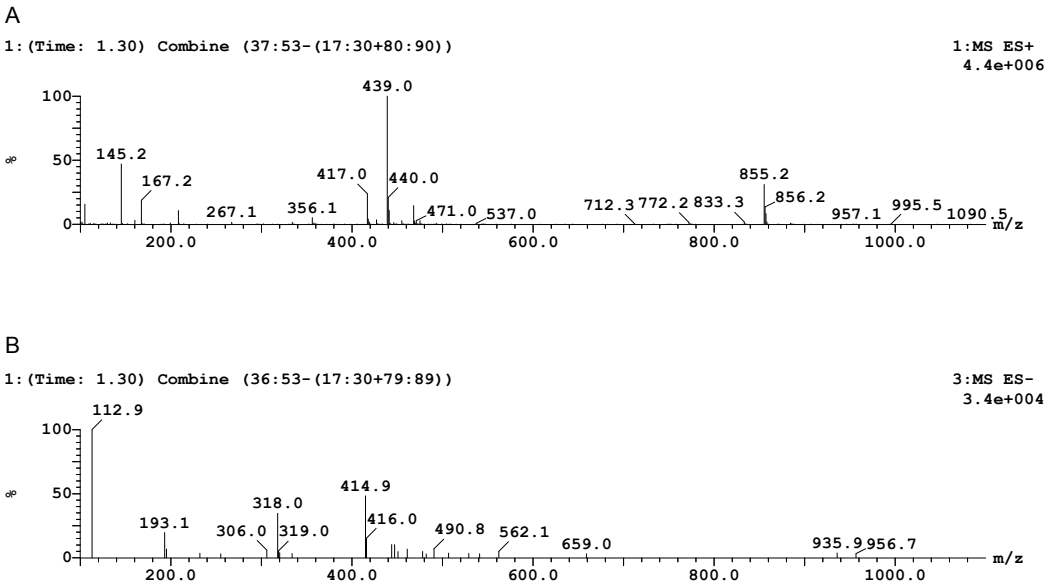

Figure 2.3 ESI-MS spectra of compound 3. (A) The $[M+H]^+$ peak is seen at m/z 417.0 in positive ion mode. Peak at m/z 439.0 corresponds to the sodium adduct of compound 3. (B) Negative ion mode spectrum shows the M^- peak for compound **2** at m/z 414.9, corresponding to the loss of a proton.

2.5 Modification of probe oligonucleotides with dithiol linker

Probe oligonucleotides (see Table 2.2) were received from the manufacturer with an amine-terminated alkyl linker. Compound **3** was dissolved in DMSO (40 μL of ~240 mM; ~9.6 μmol) and added to the oligonucleotide probe (100 μL of 500 μM; ~50 nmol) dissolved in borate buffer (25 mM, pH 8.5, ~50% DMSO). An additional 20 μL of DMSO was added to the reaction mixture, which was then left to mix for 24 h at room temperature. Borate buffer (590 μL) was added to the reaction mixture to precipitate excess **3**. The mixture was centrifuged to pellet the precipitate and the supernatant was then loaded onto a NAP-10 column to remove any residual **3**. Oligonucleotide probe was quantified by UV-visible spectrophotometry, split into 20 nmol fractions, and each fraction was concentrated to dryness under vacuum, then stored at −20 °C.

2.6 Labeling block oligonucleotides with fluorescent dye

Block oligonucleotides (see Table 2.2) were received from the manufacturer with thiol linkers protected as disulfides.

Labeling of Block 2 with A680

The disulfide of the as-received oligonucleotide (50 nmol) was reduced in 100 μL of tris(2-carboxyethyl)-phosphine (TCEP; 123 mM) in nuclease-free water for 1 h. The TCEP was removed by size-exclusion chromatography (SEC) with a NAP-10 column (GE Healthcare, Baie-d'Urfé, QC, Canada) using PBS (10mM, pH 7.0, 50 mM NaCl) following the manufacturer's instructions. The oligonucleotide fraction of the column eluate was immediately added to 15 μL of Alexa Fluor 680 C2 maleimide (11.1 mg mL^{-1}, ~170 nmol) in DMF. The reaction mixture was vortexed and then agitated for 21 h at room temperature while protected from light. Dye-labeled oligonucleotide was purified from excess dye through SEC with a Bio-Gel P-6 (Bio-Rad; Mississauga, ON, Canada) column using TEAA buffer (5 mM, pH 7.0). The purified A680-labeled Block 2 (Blk 2) oligonucleotide and its degree of labeling (~1:1) were quantified by UV-visible spectrophotometry, split into 10 nmol fractions, and each fraction concentrated to dryness under vacuum, then stored at −20 °C.

Labeling of Block 1 with A633

Oligonucleotide (~50 nmol) was dissolved in 50 μL of water with 4% v/v triethylamine. Aqueous dithiothreitol (50 μL, 100 mM) was added and the mixture left at room temperature for 25 min. The solution was then extracted with six 400 μL portions of wet ethyl acetate. The aqueous phase was retained and diluted with 50 μL of PBS (100 mM, pH 7.4) before adding 15 μL of Alexa Fluor 633 C5 maleimide (11.1 mg mL^{-1}, ~130 nmol) in DMF. The reaction mixture was vortexed and then agitated for 20 h at room temperature while protected from light. The A633-labeled oligonucleotide was purified and quantitated as described above for labeling Block 1 (Blk 1) with A680.

2.7 Conjugation of QDs with oligonucleotide probe

QD605 (100 μL, 1 μM) were mixed with *P* equiv. of each dithiol-terminated linker-modified probe oligonucleotide (Prb 1, Prb 2) in tris-borate buffer (400 mM, pH 7.4, 50 mM NaCl) with TCEP (10 mM) for 20 h at room temperature. After this time, additional TCEP was added (2 μL, 100 mM) and the NaCl concentration was increased to 400 mM (with addition of a 5 M stock solution; referred to as "salt aging"). The mixture was left at room temperature for an additional 9 h. Unconjugated probe oligonucleotides were removed by purification on a Sephacryl S300 column with borate buffer (16 mM, pH 8.5) as the eluent. Typical reaction scales were between 100–300 μL. A 9 cm × 6 mm (length × diameter) column was sufficient for purification. Successful separation of unconjugated oligonucleotides was confirmed by UV-visible spectrophotometry. For hybridization assays described in Section 2.8 (data presented in Figure 3.15), QD-probe oligonucleotide conjugates were prepared with $P = 15$ equiv. for both probes. For displacement assays described in Section 2.9 (data presented in Figure 3.17), the QD-probe oligonucleotide conjugates were prepared with $P = 10$ equiv. for both probes.

2.8 Hybridization assays

QD-probe oligonucleotide conjugates (40 μL, 50 nM) were incubated with the desired number of equivalents of dye-labeled block sequences in tris-borate buffer (200 mM, pH 7.4, 200 mM NaCl) for 1 h. PL emission spectra were measured by loading 35 μL of sample into the wells of a 384-well plate. The excitation wavelength was 464 nm and emission was measured between 500–850 nm (2 nm step size).

2.9 Displacement assays

QD-probe oligonucleotide conjugates (100 nM) were mixed and hybridized with 10 equiv. of Blk 1(A633) and Blk 2(A680) in tris-borate buffer (200 mM, pH 7.4, 200 mM NaCl) for 1.5–2 h. Next, 20 μL aliquots of the block-hybridized conjugates were added to

20 μL volumes of solutions with different numbers of equivalents of Tgt 1 and Tgt 2. After mixing, the samples were left at room temperature for 1 h (the final concentration of QD conjugates was 50 nM). PL emission spectra were measured as noted for the hybridization assays.

2.10 Data analysis and crosstalk corrections

2.10.1 Crosstalk corrections

There was some crosstalk between the QD605 PL and the A633 PL, and between the A633 PL and A680 PL. This crosstalk was corrected prior to the calculation of PL ratios.

Let the peak PL emission intensity of a QD or dye, X, to be ${}_{X}I$. The raw PL intensity measured at a wavelength λ is defined as $I_{\lambda(\mathrm{nm})}$. For QD605–$(A633)_M$ samples with M equivalent(s) of A633 labeled peptides per equivalent of QDs, the crosstalk corrected PL intensities for the QD605 and A633 were calculated according to eqns. 2.1–2.2, where ${}_{X}\sigma_{\lambda}$ is a correction factor. The value of ${}_{X}\sigma_{\lambda}$ was determined from the PL emission spectrum of X, and represents the PL intensity at wavelength λ relative to the peak PL intensity of X at its emission maximum ($0 < {}_{X}\sigma_{\lambda} < 1$). The correction factors were ${}_{QD}\sigma_{648}$ = 0.018, ${}_{A633}\sigma_{604}$ = 0.008, ${}_{A680}\sigma_{648}$ = 0.011, and ${}_{A633}\sigma_{704}$ = 0.272. In some cases, consideration of only ${}_{QD}\sigma_{648}$ and ${}_{A633}\sigma_{704}$ was sufficient.

$$ {}_{QD}I = I_{604} - {}_{A633}\sigma_{604}({}_{A633}I) \tag{2.1} $$

$$ {}_{A633}I = I_{648} - {}_{QD}\sigma_{648}({}_{QD}I) \tag{2.2} $$

Eqns. 2.1–2.2 are a system of two equations and two unknowns that can be solved, which results in eqn. 2.3. Calculation of eqn. 2.3 permits direct calculation of eqn. 2.1.

$$ {}_{A633}I = \frac{I_{648} - {}_{QD}\sigma_{648}(I_{604})}{1 - {}_{QD}\sigma_{648}({}_{A633}\sigma_{604})} \tag{2.3} $$

For QD605–$(A680)_N$ samples with N equivalent(s) of A680 labeled peptides per

equivalent of QDs, the PL emission peaks were sufficiently resolved that no crosstalk correction was necessary, as formalized by eqns. 2.4–2.5.

$$ {}_{QD}I = I_{604} \tag{2.4} $$

$$ {}_{A680}I = I_{704} \tag{2.5} $$

For QD605–$(A633)_M$–$(A680)_N$ samples, crosstalk between QD605 and A633, and between A633 and A680, was corrected using eqns. 2.1, 2.6 and 2.7, which are a system of three equations and three unknowns:

$$ {}_{A633}I = I_{648} - {}_{QD}\sigma_{648}({}_{QD}I) - {}_{A680}\sigma_{648}({}_{A680}I) \tag{2.6} $$

$$ {}_{A680}I = I_{704} - {}_{A633}\sigma_{704}({}_{A633}I) \tag{2.7} $$

Eqns. 2.1, 2.6, and 2.7 can be solved to yield eqn. 2.8. Calculation of eqn. 2.8 permits direct calculation of eqns. 2.1 and 2.7.

$$ {}_{A633}I = \frac{I_{648} - {}_{QD}\sigma_{648}(I_{604}) - {}_{A680}\sigma_{648}(I_{704})}{1 - {}_{QD}\sigma_{648}({}_{A633}\sigma_{604}) - {}_{A680}\sigma_{648}({}_{A633}\sigma_{704})} \tag{2.8} $$

Peak PL intensity ratios, $\rho_{\text{dye/QD}}$, were calculated according to eqns. 2.9 and 2.10:

$$ \rho_{A633/QD} = {}_{A633}I / {}_{QD}I \tag{2.9} $$

$$ \rho_{A680/QD} = {}_{A680}I / {}_{QD}I \tag{2.10} $$

2.10.2 Data analysis

Peak PL intensity ratios, $\rho_{\text{A633/QD}}$ and $\rho_{\text{A680/QD,}}$ calculated as described in Section 2.10.1 were plotted versus the number of A633 (M) per QD and A680 per QD (N) to construct a calibration plot. Such calibration plots could be analyzed either as two-dimensional plots in Figure 3.6B and Figure 3.15C, or as three-dimensional plots in Figure 3.16 A and B.

In the case of target displacement assays, where calibration plots of $\rho_{A633/QD}$ and $\rho_{A680/QD}$ were used to determine the amounts of target 1 (x) and target 2 (y) in the blinded unknown samples, both calibration plots could be expressed as mathematic functions for a system of two equations to be solved for determining unknown x and y. Solver (Microsoft Excel analysis tool) was used to solve for x and y by minimizing the sum of the square of differences between the measured and calculated values of each of $\rho_{A633/QD}$ and $\rho_{A680/QD}$. The constraints of x and y in Solver analysis were set to be consistent with the constraints in the calibration plots.

2.11 Gel electrophoresis

A 2 μL volume of 50% v/v (*aq*) glycerol was mixed with a 10 μL volume of conjugate sample before loading 12 μL into a well of a 1.0% w/v agarose gel. The gel was run at a field-strength of 6.7 V cm^{-1} for *ca.* 25–30 min at room temperature in tris-borate buffer (100 mM, pH 8.3).

2.12 PL lifetime measurements

Time-resolved PL measurements were made with a streak camera system. Samples in a quartz cuvette were excited with laser pulses from an optical parametric generator (EKSPLA, Vilnius, Lithuania) pumped by a pulsed laser at 355 nm with a 10 Hz repetition rate and 35 ps pulse duration (EKSPLA). Time-resolved spectra were recorded with a combination of a spectrograph (Princeton Instruments, Trenton, NJ, USA) and streak camera (C7700; Hamamatsu Photonics, Hamamatsu, SZK, Japan) in photon counting mode. The excitation wavelengths were 464 nm for QD605, 570 nm for A633, and 610 nm for A680.

2.13 Average signal-to-background ratios

To compare the utilities of the QD605–A633–A680 and QD520/QD525a–A555–A647 cFRET configurations in serum and blood matrices, the average signal-to-background (S/B) ratios were calculated for the four samples: (0, 0), (12, 0), (0, 12), and (12, 12). The signal-to-background ratio was calculated for each sample at each wavelength in three

steps. First, the measured PL spectrum for the serum or blood matrix was subtracted from the measured PL spectrum for a (*M*, *N*) configuration. This background-corrected spectrum was then divided by the PL spectrum for the matrix at each wavelength. Finally, the resulting S/B ratios for the four samples were averaged at each wavelength. These averaged values are plotted in Figure 3.11.

2.14 Quantum yield measurements

Unknown quantum yields (Φ_X) were determined relative to reference standards (Φ_{std}) by plotting measured fluorescence intensities (*F*) versus measured absorbance values (*A*) at the excitation wavelength. Eqn. 2.11 shows how the slopes of these plots relate to the quantum yields, where η is the refractive index of the solvent. Fluorescein was measured in 0.10 M NaOH (*aq*), and sulfo-Cy5 quantum yield was measured in ethanol as standards. All other quantum yields were measured in aqueous buffer.

$$\Phi_X = \Phi_{std} \frac{F_X}{A_X} \frac{A_{std}}{F_{std}} \frac{\eta_X^2}{\eta_{std}^2} \tag{2.11}$$

Chapter 3
Results and Discussion

3.1 Results

3.1.1 Spectra

To characterize the spectroscopic properties of QD605, A633 and A680, both their normalized absorption (dotted line) and emission spectra (solid line) were measured and are shown in Fig. 3.1. Table 3.1 shows the important spectroscopic parameters of the three fluorophores. The peak PL wavelengths of QD605, A633 and A680 are well separated from each other (604 nm, 648 nm and 704 nm) to help reduce spectral crosstalk. As shown in both Fig. 3.1A and Table 3.1, there is significant spectral overlap between the emission spectrum of the QD605 donor and the absorption spectra of each of the acceptor dyes A633 ($J_{QD605\text{-}A633}$ = 8.3×10^{-10} cm^6 mol^{-1}) and A680 ($J_{QD605\text{-}A680}$ = 6.4×10^{-10} cm^6 mol^{-1}), with even more pronounced spectral overlap between A633 and A680 ($J_{A633\text{-}A680}$ = 19×10^{-10} cm^6 mol^{-1}). The large molar absorption coefficient of QD605 at *ca.* 400-475 nm offers an efficient excitation region where the acceptor dyes A633 and A680 absorb minimally (Fig. 3.1A and pointed arrow in Fig. 3.1B) to minimize direct excitation of the dyes.

Overall, the photophysical properties of the long-wavelength QD605–A633–A680 cconfiguration fulfill requirements for a cFRET configuration, which are an efficient excitation region for the QD with minimal direct excitation of both acceptor dyes, significant spectral overlap (for FRET) between the donor and acceptor pairs, and sufficient spectral separation between the emission of QD and both dyes.

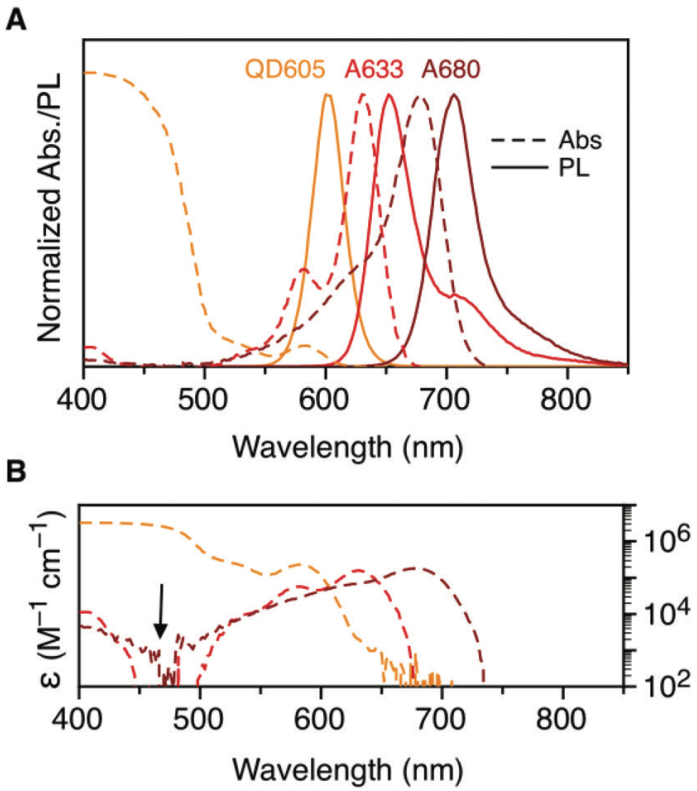

Figure 3.1 Absorption and PL spectra of QD605, A633 and A680. (A) Normalized absorption (dotted line) and PL emission spectra (solid line) for QD605, A633, and A680. (B) Absorption spectra in panel A re-plotted as the wavelength-dependent molar absorption coefficient, $\varepsilon(\lambda)$. The arrow indicates the preferred excitation wavelength for the QD605-A633-A680 cFRET system. Note the logarithmic scale in panel B. Reproduced from ref.[48] by permission of The Royal Society of Chemistry. Copyright 2016

Table 3.1 QD and dye properties

Properties	QD605	A633	A680
λ_{Abs} [a] (nm)	584	630	678
ε [b] (10^3 M^{-1} cm^{-1})	232	159	183
λ_{PL} [c] (nm)	604	648	704
Φ [d]	0.23	0.45	0.31
τ [e] (ns)	12.7	1.0	0.4
$J_{X\text{-}A633}$ [f] (10^{-10} cm^6 mol^{-1})	8.3	-	-
$R_{0,\ X\text{-}A633}$ [g] (nm)	5.7	-	-
$J_{X\text{-}A680}$ [f] (10^{-10} cm^6 mol^{-1})	6.4	19	-
$R_{0,\ X\text{-}A680}$ [g] (nm)	5.5	7.4	-

[a] First excition peak for the QD605 and absorption maximum for the dyes. [b] Peak molar absorption coefficient. [c] Peak PL wavelength. [d] Quantum yield of the QD or dye-oligonucleotide conjugate. [e] PL lifetime (amplitude weighted average lifetime for QD605). [f] Spectral overlap integral. [g] Forster distance. Reproduced from ref.[48] by permission of The Royal Society of Chemistry. Copyright 2016.

3.1.2 Photophysical properties of QD605-A633-A680 cFRET configuration

Quantum yields

For the QD605, the reference standard was fluorescein in 0.10 M NaOH (*aq*) (Φ = 0.79) and both emitters were excited at 464 nm.[52] For the A680 and A633, the quantum yield was measured with sulfo-Cy5 as the reference standard (Φ = 0.20 as per the manufacturer; Lumiprobe Inc., Hallandale Beach, FL, USA) and excitation at 600 nm. The measured quantum yields are tabulated in Table 3.1. The raw data is shown in Figure 3.2. The measured value for Blk 2(A680) (Φ = 0.31) was close to the value reported by the manufacturer (Φ = 0.36; Thermo-Fisher). The manufacturer does not report a value for A633.

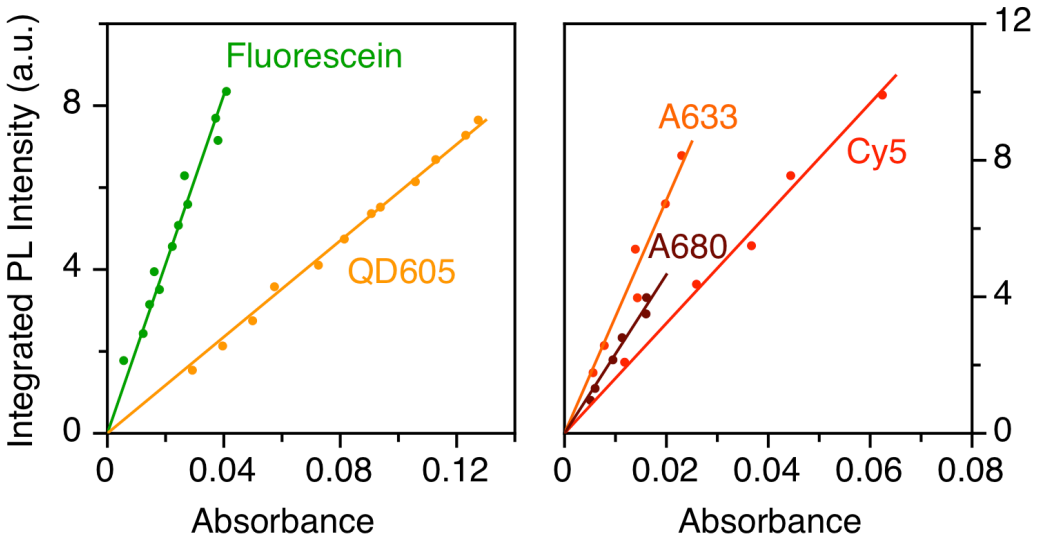

Figure 3.2 Plots of integrated PL intensity versus absorbance for (left) QD605 with a fluorescein reference, and (right) A633 and A680 with a sulfo-Cy5 reference. Reproduced from ref.[48] by permission of The Royal Society of Chemistry. Copyright 2016.

PL lifetimes

PL lifetimes for the QD605, A633, and A680 are listed in Table 3.1. PL intensity decay curves are shown in Figure 3.3. The QD605 PL decay was fit with a biexponential lifetime (2.6 ns, 16%; 14.6 ns, 84%) and the amplitude weighted average lifetime is given in Table 3.1. The PL decays of the dyes were adequately fit with monoexponential lifetimes.

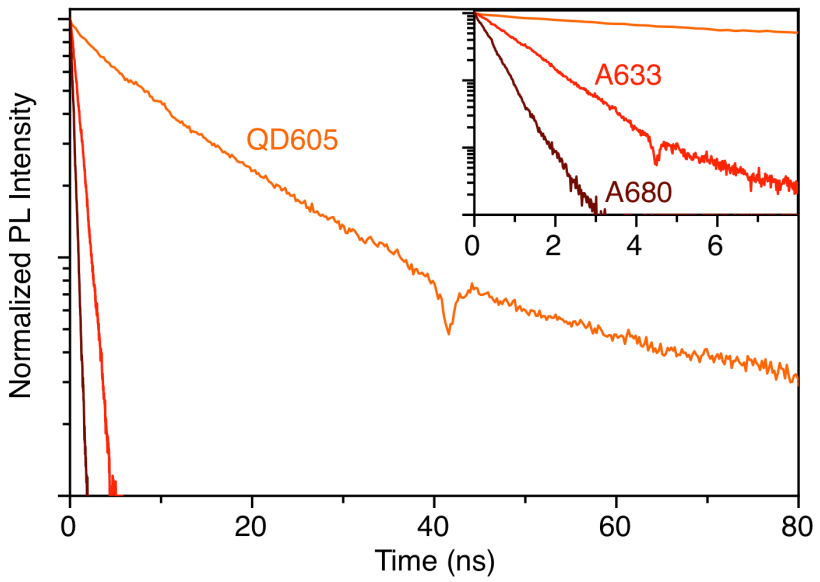

Figure 3.3 PL decay curves for directly excited QD605, Pep(A633), and Pep(A680). The dip in the data near 40 ns (and 4 ns in the inset) is a detector artifact. The inset is an expanded view of the data between 0–8 ns. Reproduced from ref.[48] by permission of The Royal Society of Chemistry. Copyright 2016.

3.1.3 cFRET spectra and PL ratios

To study the QD605-A633-A680 cFRET configuration, an array of QD605–$[Pep(A633)]_M$–$[Pep(A680)]_N$ samples were prepared, where M specifies the average number of Pep(A633) per QD, and N specifies the average number of Pep(A680) per QD. Each configuration is abbreviated as (M, N), where $0 \leq M \leq 12$ and $0 \leq N \leq 12$. The assembly of dye-labeled peptides onto QD605 was confirmed by running gel electrophoresis on samples of (0, 0), (3, 3), (6, 6), (9, 9) and (12, 12) as shown in Figure 3.4. The electrophoretic mobility of the QD605–$[Pep(A633)]_M$–$[Pep(A680)]_N$ conjugates decreased as M and N increased. The emission spectra of all configurations were recorded at a chosen excitation wavelength of 464 nm, and are shown in Figure 3.5. Spectra from configurations with only one type of dye assembled on the QD, as in Figure 3.5A and all $N = 0$ spectra across Figure 3.5A–E, show that both A633 and A680 were effective FRET acceptors to QD605. As more acceptor dyes were assembled, the QD PL was quenched and FRET-sensitized acceptor dye PL increased. Figure 3.5F shows the negligible PL

from direct excitation of each acceptor dye at 464 nm, further confirming the effective FRET-sensitized PL of both acceptor dyes from QD. Quenching efficiencies data from (M, 0) and (0, N) samples suggest a distance of 6.60–7.05 nm between dye acceptor and centre of the QD core according to FRET formalism in eqn. 1.10.

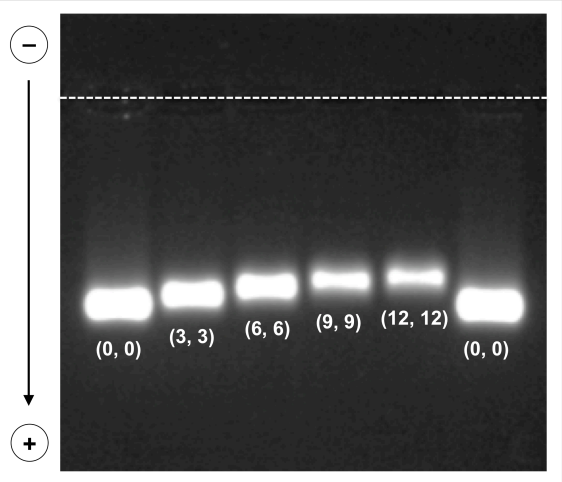

Figure 3.4 PL image of an agarose gel showing changes in the electrophoretic mobility of QD605–$[Pep(A633)]_M$–$[Pep(A680)]_N$ conjugates as the values of M and N increase. The average number of each peptide per QD is indicated by (M, N). The dashed line marks the position of the sample wells. The polarity of the applied electric field is indicated at the left along with the direction of migration. Reproduced from ref.[48] by permission of The Royal Society of Chemistry. Copyright 2016.

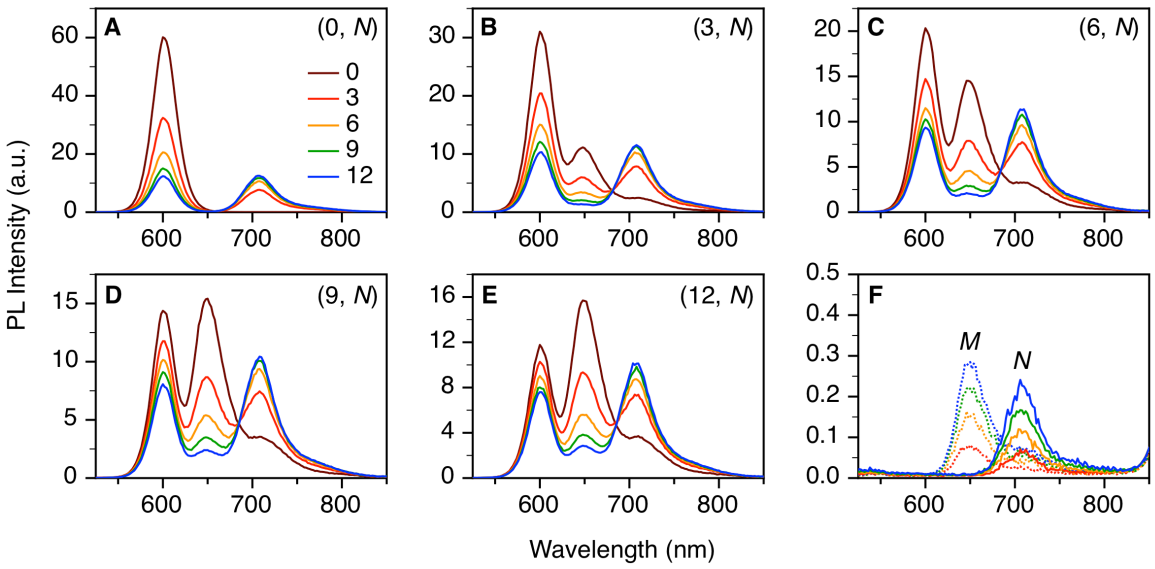

Figure 3.5 PL emission spectra (464 nm excitation). (A)-(E) PL spectra of QD605–$[Pep(A633)]_M$–$[Pep(A680)]_N$ cFRET configurations. (F) The corresponding *M* × Pep(A633) and *N* × Pep(A680) samples. The configurations are denoted by the shorthand (*M, N*) notation. The legend in panel A applies to all other panels. Note the difference in the PL intensity scale for panel F. Reproduced from ref.[48] by permission of The Royal Society of Chemistry. Copyright 2016.

When both types of acceptor dyes were assembled onto the QD, sequential and competitive pathways took place, leading to energy distribution patterns that depended on and were unique to a specific (*M*, *N*) configuration. Such energy distributions were reflected by A633/QD605 and A680/QD605 PL ratios that were derived from the ensemble PL intensities of QD605, A633, and A680 for particular (*M*, *N*) of a QD605–$[Pep(A633)]_M$–$[Pep(A680)]_N$ configuration.

Spectra for the (12, *N*) cFRET configurations in Figure 3.6A show that increases in the number of assembled A680 at a fixed number of A633 on QD605 quenched both the QD605 and A633 PL by enhancing the competitive pathway as well as by adding acceptors for A633 in the sequential pathway. Increases in the number of assembled A680 introduced additional dye acceptors that competed with A633 for energy from QD605 in the competitive pathway. Meanwhile, additional A680 caused further quenching of A633 by enhancing energy transfer from A633 to A680. As shown in (*M*, 12) in Figure 3.6A, increases in the number of assembled A633 quenched both QD605 PL and A680 PL by adding A633 acceptors that competed with A680. In

principle, increases in the number of A633 should add more donors for relaying energy to A680 in the sequential pathway. However, the overall slight decrease in A680 PL when A633 was added showed that the competition between A633 and A680 for energy transfer from QD605 is more potent than the A633-to-A680 sequential pathway.

The dynamics of these energy transfer processes lead to plots of A633/QD605 PL ratio and A680/QD605 PL ratio that display unique trends with respect to the values of *M* and *N* as shown in Figure 3.6B. A633/QD605 PL ratio increases with increasing number of A633 per QD605, decreases with increasing number of A680 per QD605. A680/QD605 PL ratio increases with increasing number of A680 per QD605, while it decreases with increasing number of A633 per QD605. These trends within the cFRET system then lead to unique combinations of A633/ QD605 and A680/ QD605 PL ratios that correspond to each (*M*, *N*) configuration as shown in Figure 3.6C.

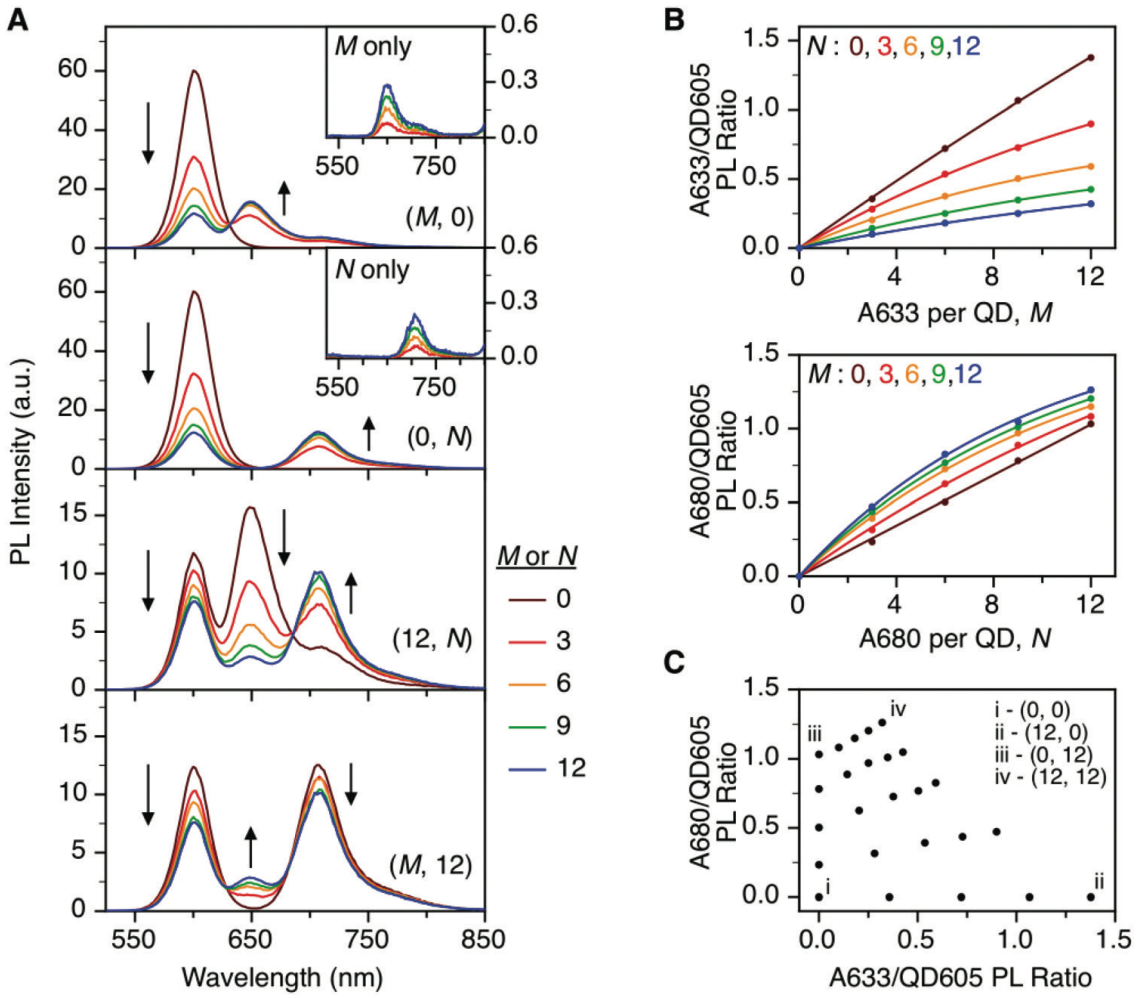

Figure 3.6 Trends in photoluminescence ratios. (A) Representative PL emission spectra for (*M*, *N*) = (*M*, 0), (0, *N*), (12, *N*), and (*M*, 12) QD605–[Pep(A633)]$_M$–[Pep(A680)]$_N$ cFRET configurations. The insets show PL spectra for control samples of Pep(A633) (*M* only) and Pep(A680) (*N* only) without QD605. (B) Summary of the A633/QD605 and A680/QD605 PL ratios as a function of *M* and *N*. (C) Plot showing that each (*M*, *N*) yields a unique combination of A633/QD605 and A680/QD605 PL ratios. Reproduced from ref.[48] by permission of The Royal Society of Chemistry. Copyright 2016.

3.1.4 cFRET efficiencies

In the QD605–[Pep(A633)]$_M$–[Pep(A680)]$_N$ cFRET configuration, both QD605 and A633 act as donor to relay in energy transfer processes. Studying quenching efficiencies of the energy donors assist in understanding and confirming the energy transfer pathways proposed for the cFRET configuration in Figure 1.7A.

As mentioned in Section 1.2.3, the quenching efficiency of QD in a cFRET configuration

is related to the rates of QD605-to-A633 energy transfer pathway and the QD605-to-A680 energy transfer pathway as shown in eqn. 3.1.

$$Q_{QD605} = \frac{Mk_{QD605}^{-1}k_{QD605-A633} + Nk_{QD605}^{-1}k_{QD605-A680}}{1 + Mk_{QD605}^{-1}k_{QD605-A633} + Nk_{QD605}^{-1}k_{QD605-A680}} \quad (3.1)$$

Experimental values of rates of these two energy transfer pathways were calculated from data of (M, 0) and (0, N) configurations shown in Figure 3.7A (i) and (ii), and used to construct plot in Figure 3.7A (iii) to compare the experimental QD quenching efficiencies with the predicted values. The slope close to unity suggests that the QD605–$[\text{Pep(A633)}]_M$–$[\text{Pep(A680)}]_N$ configuration follows the expected energy transfer dynamics of a cFRET configuration.

When studying the quenching efficiency of A633 in the A633-to-A680 energy transfer pathway, both the A633-to-A680 sequential pathway and the QD605–A680 competitive pathway need to be considered. In Figure 3.7B, plot with solid circles demonstrate the quenching efficiency of A633, Q_{A633}, in QD605–$[\text{Pep(A633)}]_M$–$[\text{Pep(A680)}]_N$ cFRET configuration when exciting QD605 at 464 nm. The quenching efficiency of A633 is based on when $N = 0$ for each value of M. The Q_{A633} ranges from *ca.* 40% to 90%. The energy transfer pathway of A633-to-A680 could be isolated by excitation at 620 nm, a wavelength longer than the first exciton peak of QD605, to minimize excitation of the QD605, and thus to minimize FRET from QD605 to A633 or A680 to avoid the competitive energy transfer pathways. The empty circles in Figure 3.7B shows the experimental energy transfer efficiency, $E_{\text{A633-A680}}$ (exp.) of A633 with excitation at 620 nm. The $E_{\text{A633-A680}}$ (exp.) is at maximum *ca.* 23 ± 3% at $N = 12$, which is much smaller than Q_{A633}. To account for the difference between Q_{A633} and $E_{\text{A633-A680}}$ (exp.), quenching of A633 due to the competitive energy transfer pathway, $Q_{\text{A633-c}}$, was predicted through eqn. 3.2 shown below. Eqn. 3.2 implies that the quenching of A633 due to the QD605-A680 competitive pathway equals to the quenching efficiency of the QD605 due to QD605-A680 pathway.

$$Q_{A633-c} = 1 - \frac{1 + Mk_{QD-A633}k_0^{-1}}{1 + Mk_{QD-A633}k_0^{-1} + Nk_{QD-A680}k_0^{-1}} \tag{3.2}$$

Subtracting the predicted $Q_{\text{A633-c}}$ from experimental Q_{A633} yields the predicted $E_{\text{A633-A680}}$ at excitation wavelength of 464 nm, shown as dotted lines in shaded region of Figure 3.7B. The fact that the experimental $E_{\text{A633-A680}}$ with excitation at 620 nm is only at the bottom edge of the shaded region could be attributed to the non-negligible amount of direct excitation of A680 at 620 nm. Excited A680 is not available for accepting energy from A633. At 620 nm, A680 with molar absorption coefficient of *ca.* 63 000 M^{-1} cm^{-1} is more than half as likely as A633 (*ca.* 117 000 $M^{-1}cm^{-1}$) to be excited. Therefore, the non-negligible reduction in the number of ground-state A680 in A633-to-A680 energy transfer pathway at 620 nm shifts the experimental $E_{\text{A633-A680}}$ downward from the calculated $E_{\text{A633-A680}}$.

In summary, the study of quenching efficiencies of both QD605 and A633 confirms the competitive and sequential energy transfer pathways in a cFRET configuration depicted in Figure 1.7A.

3.1.5 cFRET photobleaching

One of the important properties of a cFRET configuration is its resistance to photobleaching. In biosensing applications that require spatial information, signal acquisition with a microscope would expose the cFRET probe to a light source that operates at sufficient intensity to potentially photobleach the system within the intended time period of experiment. An experiment to study the resistance of QD605–$[\text{Pep(A633)}]_M$–$[\text{Pep(A680)}]_N$ cFRET configuration to photobleaching, and compare it to that of the well-studied QD520-A555-A647 cFRET configuration provides insight on the functional properties of the cFRET configurations. Photobleaching also acts as an off-switch for acceptor dyes and the corresponding change in the PL of other optical components can reveal energy transfer pathways.

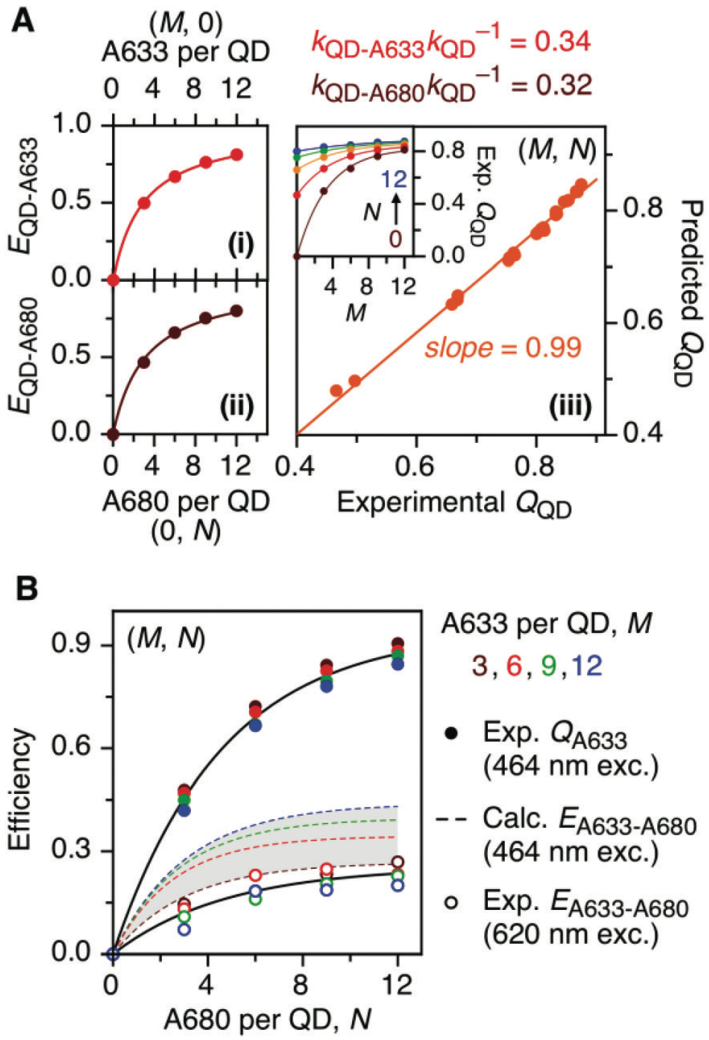

Figure 3.7 FRET and cFRET efficiencies. (A) Efficiencies, E_{QD-X}, for (i) QD-to-A633 FRET measured from (*M*, 0) configurations and (ii) QD-to-A680 FRET measured from (0, *N*) configurations. The relative energy transfer rates, $k_{QD-X}k_{QD}^{-1}$, derived from this data are listed and can be used to predict the efficiency of QD PL quenching, QD, for (*M*, *N*) configurations, which (iii) show a good correlation with the experimentally measured quenching efficiencies. The inset shows the experimental Q_{QD} as a function of *M* and *N*. (B) Characterization of A633-to-A680 energy transfer. The solid circles plot the measured quenching of A633 PL in (*M*, *N*) configurations, Q_{A633}, relative to the corresponding (*M*, 0) configuration, with predominant excitation of the QD605 at 464 nm. This quenching is from a combination of A633-to-A680 energy transfer and the competition between A633 and A680 to accept energy from the QD605. The latter can be calculated from the data in panel A and used to estimate the efficiencies of A633-to-A680 energy transfer, $E_{A633–A680}$ (calc.), which are shown as dashed coloured lines within the shaded region. The open circles plot the measured A633-to-A680 energy transfer efficiency, $E_{A633–A680}$ (exp.), with direct excitation of the A633 (and, to a lesser extent, A680) at 620 nm. Reproduced from ref.[48] by permission of The Royal Society of Chemistry. Copyright 2016.

Each of the four samples of (0, 0), (12, 0), (0, 12) and (12, 12) was illuminated at 450 nm with the light source from fluorescence microscope for a continuous period of 30 min. The PL spectra of the QD605, A633 and A680 were recorded at regular time intervals. Figure 3.8 shows the PL of QD605, A633, and A680 relative to their initial PL in these samples at time 0 min. Figure 3.9 shows data from the QD520-A555-A647 configuration. In Figure 3.8A, QD605 in (0, 0) sample maintained its PL close to 100% with very slight variations during 30 min of light exposure at ~98 mW (full light intensity). QD605 in all samples of (12, 0), (0, 12) and (12, 12) shows increase in PL due to photobleaching of A633 and/or A680, and thus loss of energy acceptors. When A633 was assembled onto QD605 as in the sample of (12, 0), PL of QD605 and A633 sustained for ~1.5 min before photobleaching of A633 occurred with an approximately first-order rate constant of 0.66 min^{-1}. PL of QD605 increased along with photobleaching of A633 due to loss of QD605-A633 energy transfer pathway and the recovery of QD605 PL. Similarly, the photobleaching of A680 upon illumination leads to increase of QD605 PL in sample (0, 12), except that the photobleaching of A680 occurs immediately upon illumination with a first-order rate constant of 0.75 min^{-1}. It is worth noting that the intensity of light sources had to be reduced by ~90% to ~11mW for samples with A633 and/or A680 for PL spectra to be recorded within sufficient time period. In sample (12, 12), PL of A680 decreases immediately upon illumination due to photobleaching. Meanwhile, PL of A633 increases by about four-fold before its photobleaching occurred. The increase of A633 PL was due to the more efficient energy transfer from QD605 to A633 following the loss of the QD605-to-A680 competitive pathway as well as the loss of the A633-to-A680 sequential pathway. With photobleaching of A633 after 7 min comes the rise in PL of QD605 to six times its initial PL due to loss of the QD605-to-A633 energy transfer pathway and the subsequent recovery of QD605 PL.

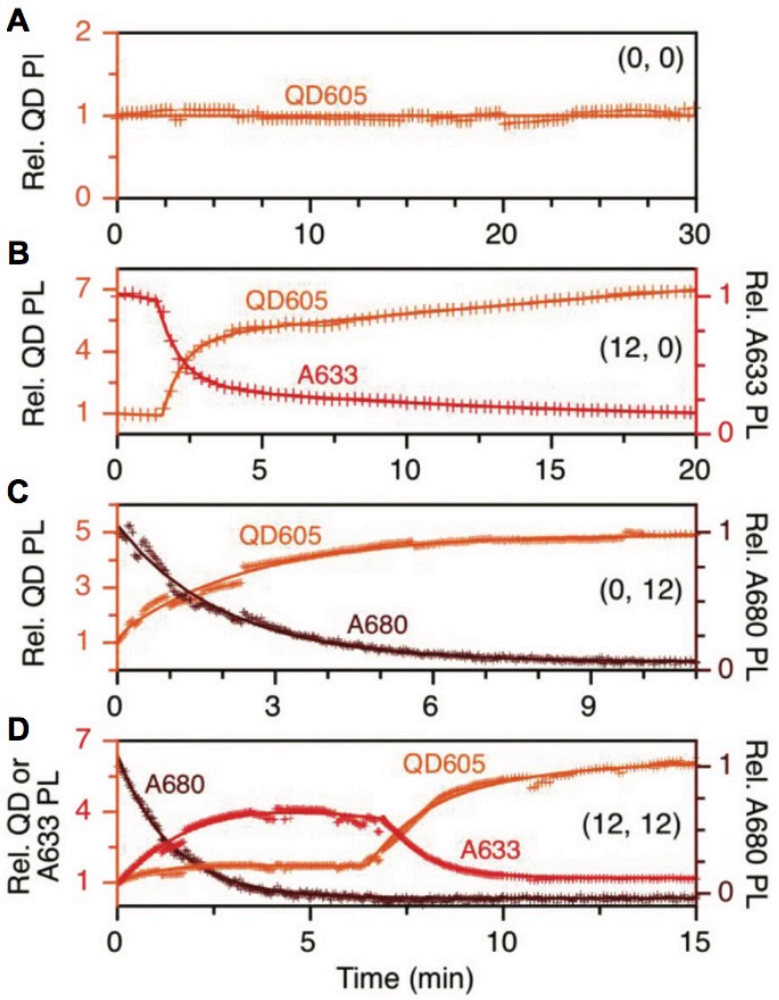

Figure 3.8 Time-dependent PL emission intensities of QD605, A633, and A680. (A) (0, 0), (B) (12, 0), (C) (0, 12), and (D) (12, 12) permutations of the QD605–$[Pep(A633)]_M$–$[Pep(A680)]_N$ cFRET configuration with continuous illumination at 450 nm. The measured power at the sample was ~11 mW, except for the (0, 0) sample, which was ~98 mW. The PL intensities are normalized to an initial value of unity. Note the two different y-axis scales (colour-coded to match the QD, A633, or A680). Adapted from ref.[48] by permission of The Royal Society of Chemistry. Copyright 2016.

Photobleaching experiments were also performed on samples of the frequently studied QD520–$[Pep(A555)]_M$–$[Pep(A647)]_N$ cFRET configuration, as a comparison to the longer-wavelength QD605–$[Pep(A633)]_M$–$[Pep(A680)]_N$ cFRET configuration. Consistent with previous results, QD520 was found resistant to photobleaching at power of ~50 mW. Taking a closer inspection at the top diagram of Figure 3.9A, QD520 displayed ~20% photobrightening before its PL reduced by ~10% of its initial value after 50 min. Illumination power was lowered by 80% to ~10 mW for all other samples. In

(12, 0) sample (Figure 3.9B), A555 PL tracked in parallel with QD520 PL, with no evidence of photobleaching of A555. In (0, 12) and (12, 12) samples, A647 bleached at a rate of 0.08 min^{-1} and 0.04 min^{-1} respectively. In the (0, 12) sample, bleaching of A647 was followed by increase of QD520 PL to twice of its initial value due to loss of QD520–A647 FRET pathway. In (12, 12) cFRET configuration in Figure 3.9D, bleaching of A647 was followed by increase of A555 PL for similar reason in QD605–$[Pep(A633)]_M$–$[Pep(A680)]_N$ cFRET configuration. After bleaching of A647, PL of QD520 and A555 became stable for the rest of the 50 min. It is worth noting that, unlike A633, which bleached subsequently after A680, the A555 did not bleach.

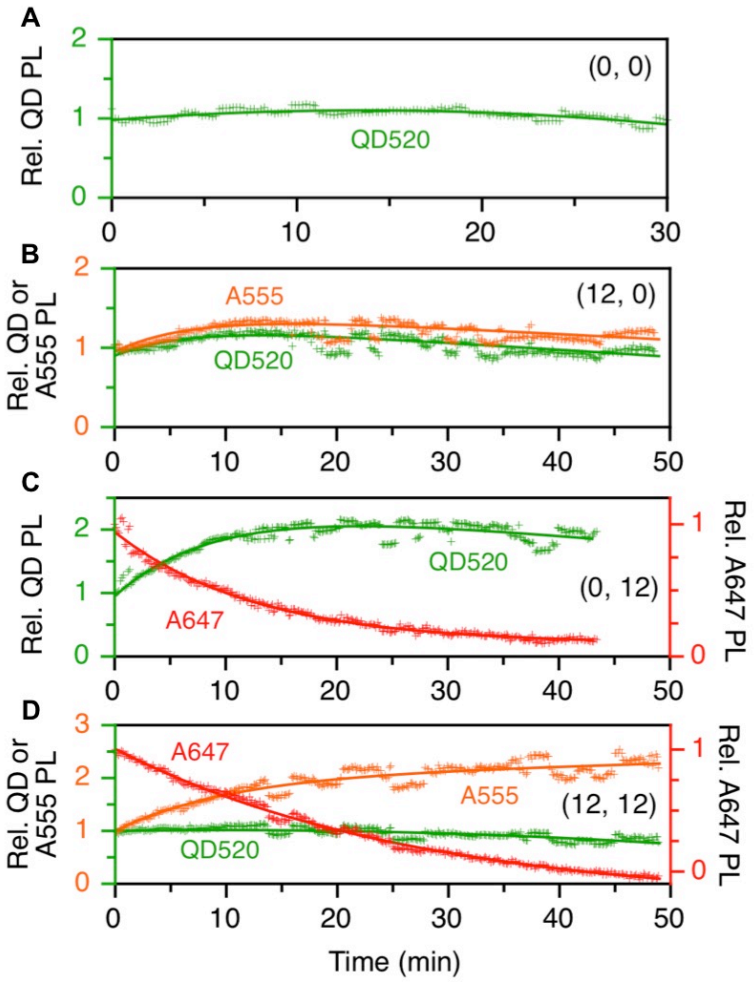

Figure 3.9 Time-dependent PL emission intensities of QD520, A555, and A647. (A) (0, 0), (B) (12, 0), (C) (0, 12) and (D) (12, 12) permutations of the QD520–[Pep(A555)]$_M$–[Pep(A647)]$_N$ cFRET configuration with continuous illumination at 400 nm are shown. The measured power at the sample was ~10 mW, except for the (0, 0) sample, which was ~50 mW. The PL intensities are normalized to an initial value of unity. (Colour-coded to match the QD520, A555, or A647). Adapted from ref.[48] by permission of The Royal Society of Chemistry. Copyright 2016.

At first glance, A633 (0.66 min^{-1}) and A680 (0.75 min^{-1}) seem to photobleach at much higher rates than A647 (0.04-0.08 min^{-1}), and therefore were more susceptible to photobleaching. However, to assess the intrinsic susceptibility to photobleaching of dyes, excitation rates need to be considered. When cFRET samples are excited at the excitation minimum for both dye acceptors, energy for excitation of dye acceptors comes primarily, in theory, through FRET-sensitization from the QD. Therefore, different excitation rates of QD605 and QD520 result in different excitation rates of the dye acceptors. Considering QD605 and QD520 have absorption coefficients of ~2 800 000 M^{-1}cm^{-1}

(450 nm) and ~114 000 $M^{-1}cm^{-1}$ (400 nm) at their excitation wavelengths for photobleaching experiments, FRET efficiencies of 80-85% for QD605 and 55-60% for QD520 yields a ~40 times higher excitation rate for QD605 than QD520. However, the observed rate of photobleaching of A647 is only ~10 times slower than A633 and A680. The discrepancy between the observed photobleaching rates and excitation rates suggest that the A633 and A680 could be ~4 times more resistant to photobleaching than A647. In the case of QDs, PL excitation spectra often significantly deviate from absorbance spectra at wavelengths ~75 nm shorter than the first exciton peak of QD, and it may therefore be suggested that the excitation rates of acceptor dyes through FRET sensitization from QD are better reflected by using the PL excitation spectra of the QD instead of the absorbance spectra. By assuming that the molar absorption coefficient applies to the first exciton peak in the PL excitation spectrum, the effective molar absorption coefficients are now extrapolated to be 418 000 $M^{-1}cm^{-1}$ for QD605 at 450 nm and 102 000 $M^{-1}cm^{-1}$ for QD520 at 400 nm. Scaling by FRET efficiencies yields excitation rates of ~6 times higher in QD605 than QD520. The corrected excitation rates suggest that A647 is ~1.5 times more resistant to photobleaching than A633 and A680.

3.1.6 Signal-to-background ratio in serum and blood matrices

One of the anticipated advantages of long-wavelength cFRET configuration was its high signal-to-background (S/B) ratio in biological samples compared to the cFRET configuration at shorter wavelength. An experiment was done to access the S/B ratios of QD605–$[Pep(A633)]_M$–$[Pep(A680)]_N$, QD520–$[Pep(A555)]_M$– $[Pep(A647)]_N$ and QD525a–$[Pep(A555)]_M$–$[Pep(A647)]_N$ cFRET configurations in matrices of buffer, 50% and 90% v/v serum, and 50% and 90% v/v blood. QD525a was chosen as an example of cFRET configuration designed with a brighter QD.

As shown in Figure 3.10B for QD520–$[Pep(A555)]_M$–$[Pep(A647)]_N$, fluorescence background of 50% serum caused obscured signals for QD520 PL in (12, 0) and both of QD520 and A555 PL in (12, 12) samples due to highly quenched QD520 and/or A555. Background noise from the matrix almost fully obscured emission spectra of all samples

in 90% serum. S/B ratios were improved when a brighter QD was used in QD525a–$[Pep(A555)]_M$–$[Pep(A647)]_N$ cFRET configuration (Figure 3.10C). Signal of (12, 12) sample in 50% serum is now much more resolved compared to that with QD520. With 90% serum, signals of (12, 0) and (12, 12) were lost in the background while signals of (0, 12) and (0, 0) remained resolved. In contrast, the QD605–$[Pep(A633)]_M$–$[Pep(A680)]_N$ cFRET configuration displayed even better S/B ratios (Figure 3.10A). Background in 50% serum caused no interference to signals in all QD605–$[Pep(A633)]_M$–$[Pep(A680)]_N$ configurations. Signals of all of QD605, A633 and A680 PL were still easily resolved in samples with 90% serum with minor background.

By comparing the wavelength-dependent average S/B ratio for all cFRET configurations in Figure 3.11B, QD605–$[Pep(A633)]_M$–$[Pep(A680)]_N$ has average S/B ratio ranging between *ca*. 4-30, higher than the average S/B ratio of QD525a–$[Pep(A555)]_M$–$[Pep(A647)]_N$ at *ca*. 0.4-4. cFRET configuration with QD520, which is less bright than QD525a, has the lowest average S/B ratio ranges between *ca*. 0.1-1. By comparing the difference between the plots of the average PL spectra in buffer with those of the average S/B ratio in 90% v/v serum for each cFRET configuration, it can be inferred that the QD605–$[Pep(A633)]_M$–$[Pep(A680)]_N$ cFRET configuration showed the best performance in terms of S/B ratios in biological samples.

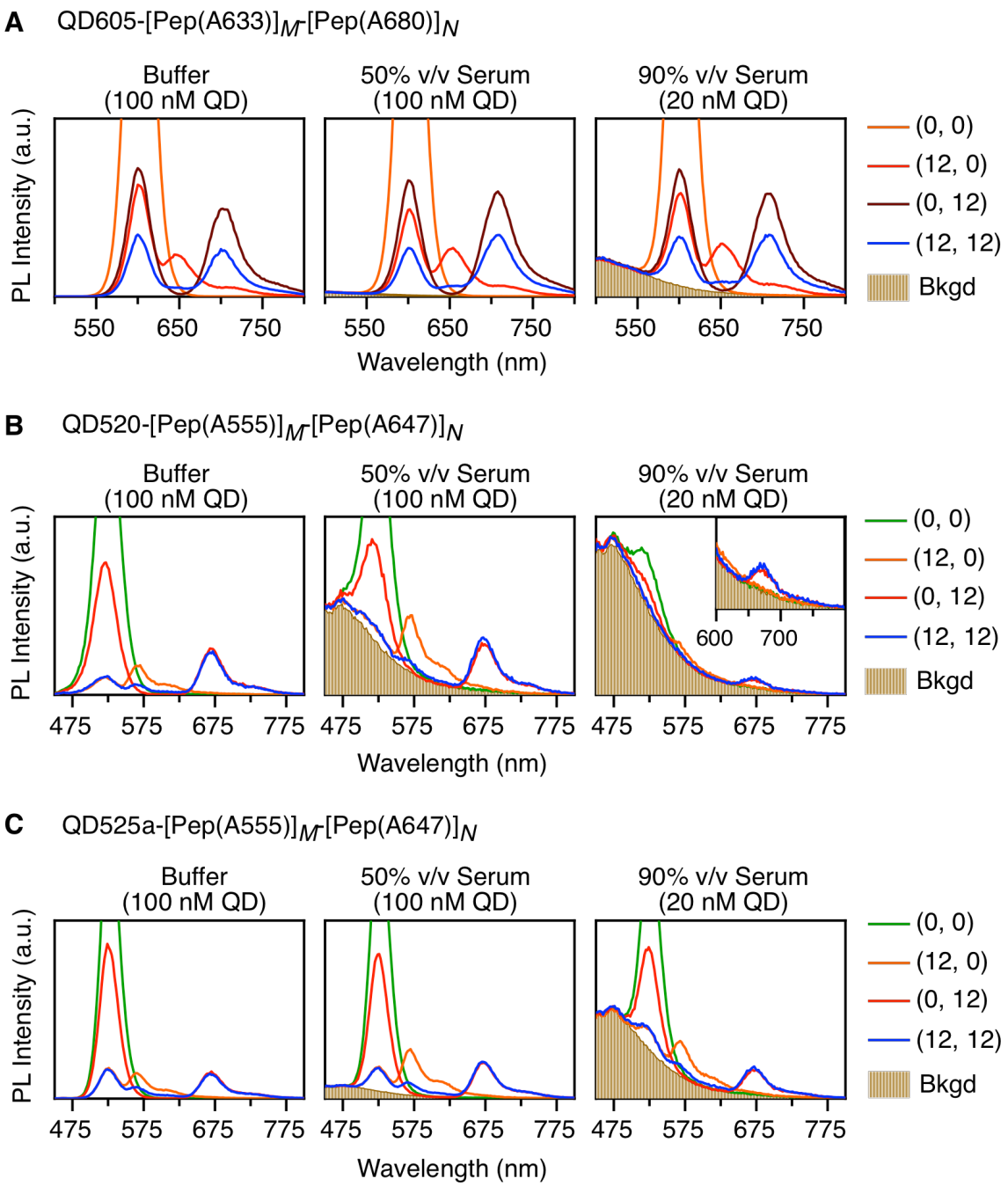

Figure 3.10 PL spectra for different cFRET configurations and permutations in buffer, 50% v/v serum, and 90% v/v serum. The intensity axis has been set so that the QD PL peaks for the (0, 0) samples are off the scale. These plots are intended to compare the signal-to-background ratios in different media and with different cFRET configurations. The scales of the intensity axes between different plots are not directly comparable. Reproduced from ref.[48] by permission of The Royal Society of Chemistry. Copyright 2016.

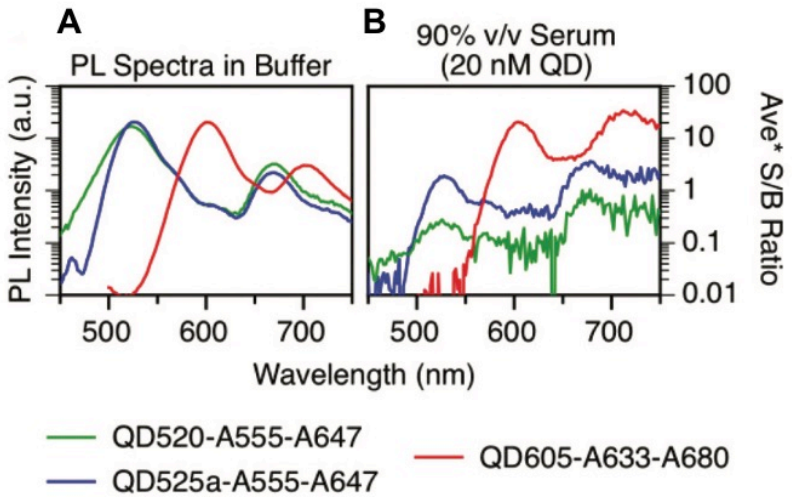

Figure 3.11 Average PL spectra and average signal-to-background (S/B) ratio. (A) Average PL spectra in buffer, plotted on a logarithmic scale, for QD520–$[Pep(A555)]_M$–$[Pep(A647)]_N$, QD525a–$[Pep(A555)]_M$–$[Pep(A647)]_N$, and QD605–$[Pep(A633)]_M$–$[Pep(A680)]_N$. (B) Average signal-to-background (S/B) ratio as a function of wavelength for these cFRET systems in 90% v/v serum. Adapted from ref.[48] by permission of The Royal Society of Chemistry. Copyright 2016.

Similar to the results in serum, the QD605–$[Pep(A633)]_M$–$[Pep(A680)]_N$ cFRET configuration achieved the best S/B ratios in whole blood media. As shown in Figure 3.12, only emission spectra of (0, 0) and (12, 0) samples of QD520–$[Pep(A555)]_M$–$[Pep(A647)]_N$ could be resolved in 50% whole blood. With the brighter green-emitting alloyed QDs, (0, 0) samples could be resolved for QD525a–$[Pep(A555)]_M$–$[Pep(A647)]_N$ in 90% blood, but spectra of other samples were interfered with noise. In contrast, emission spectra of all samples of QD605–$[Pep(A633)]_M$–$[Pep(A680)]_N$ could be resolved in up to 90% blood.

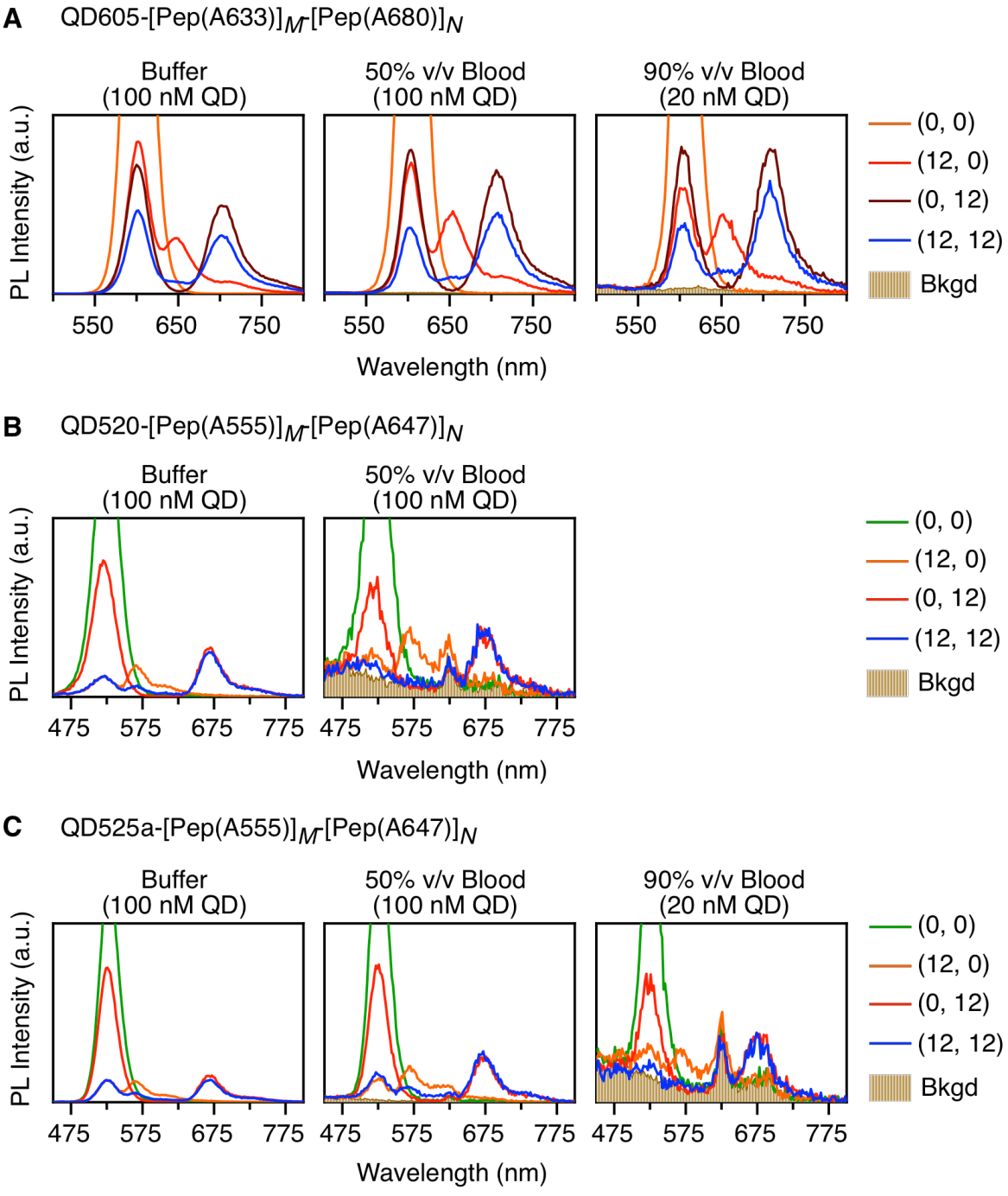

Figure 3.12 PL spectra for different cFRET configurations and permutations in buffer, 50% v/v blood, and 90% v/v blood. The intensity axis has been set so that the QD PL peaks for the (0, 0) samples are off the scale. These plots are intended to compare the signal-to-background ratios in different media and with different cFRET configurations. The scales of the intensity axes between different plots are not directly comparable. Note: 90% v/v blood was not tested for the QD520 configuration. Reproduced from ref.[48] by permission of The Royal Society of Chemistry. Copyright 2016.

3.1.7 Hybridization and target displacement assays

Experiments were done to demonstrate the utility of oligonucleotide-linked cFRET configurations for multiplexed detection of nucleic acid targets.

In a first set of experiments, QD605 was modified with dithiol linker-terminated oligonucleotide probes as QD605–[Probe 1]–[Probe 2]. Then, hybridization assays were done on QD605–[Probe 1] –[Probe 2] conjugates with partially complementary A633– or A680–labeled block sequences to correlate changes in A633/QD605 and A680/QD605 PL ratios with respect to different numbers of equivalents of A633 or A680 linked to QD605 to establish cFRET. In a second set of experiments, QD605–[Probe 1]–[Probe 2] pre-hybridized with sufficient equivalents of each of Blk 1(A633) and Blk 2(A680), which were subsequently displaced by different number of equivalents of unlabeled target strands Tgt 1 and Tgt 2 for changes in A633/QD605 and A680/QD605 PL ratios that correspond to loss of cFRET. Such changes in PL ratios were demonstrated to be useful for determination of unknown amounts of Tgt 1 and Tgt 2 in a blinded unknown experiment.

Hybridization Assay

As described in Section 2.7, dithiol linker-terminated oligonucleotide probes were incubated with QD605 in buffer in the presence of TCEP for self-assembly. Salt aging with elevated TCEP and salt concentrations was done to maximize loading of oligonucleotide probes onto the QDs. To characterize the self-assembly, PL images of agarose gel were shown in Figure 3.13. In Figure 3.13A, the decrease in electrophoretic mobility of QD605–[Probe 1]–[Probe 2] (P_1= P_2= 10 or 15) in lane (ii) and (iii) compared to the control QD605 sample in lane (i) and (v) confirmed the self-assembly of Probe 1 and Probe 2 sequences onto QD605 in the presence of TCEP, while no change in mobility was observed without TCEP in lane (iv). The requirement of TCEP as reducing agent for self-assembly confirmed that the dithiol linker acts as the anchor for the oligonucleotide to assemble on the QDs, and the oxidized disulfide form of the linker would not have affinity for the QDs. Salt aging was done to maximize the loading of

oligonucleotide probes onto the QD605. Figure 3.13B shows the mobility shift of QD605–[Probe 1]–[Probe 2] (P_1= P_2= 10) before (lane (ii)) and after salt aging (lane (iii)). As unmodified QDs tend to aggregate at high ionic strength, leading to smearing and/or poor mobility when run on gel electrophoresis, the retention of narrow band in Figure 3.13B (iii) suggests both the absence of aggregates and hence, the self-assembly of oligonucleotide probes (increased aqueous solubility and resistance to aggregation of QDs with modification of negatively charged oligonucleotides). The small decrease in mobility of the QD605 after salt aging (Figure 3.13B lane (iii)) versus lane (ii)) also suggested more oligonucleotide probes were assembled during salt aging, as the increase in size of the QD605 decreases its mobility. However, it should also be noted that such decrease in mobility of the QD due to size increase would be partially offset by the increased negative charges from the oligonucleotides.

To further assess the effect of salt aging on the assembly of more oligonucleotides onto the QD, oligonucleotide probes were hybridized with their complementary target strands in the presence of SYBR green, which is a fluorescent stain for dsDNA, to gain fluorescence signals that correspond to the quantity of the unassembled oligonucleotide probes. As shown in Figure 3.13C–D, analysis of the PL images of the agarose gel before and after salt aging showed that SYBR green fluorescence due to the unassembled oligonucleotide band decreased by ~25% relative to the PL of the QD band. The PL signal of the unassembled oligonucleotide probes after salt aging decreased by ~20% relative to the control lanes.

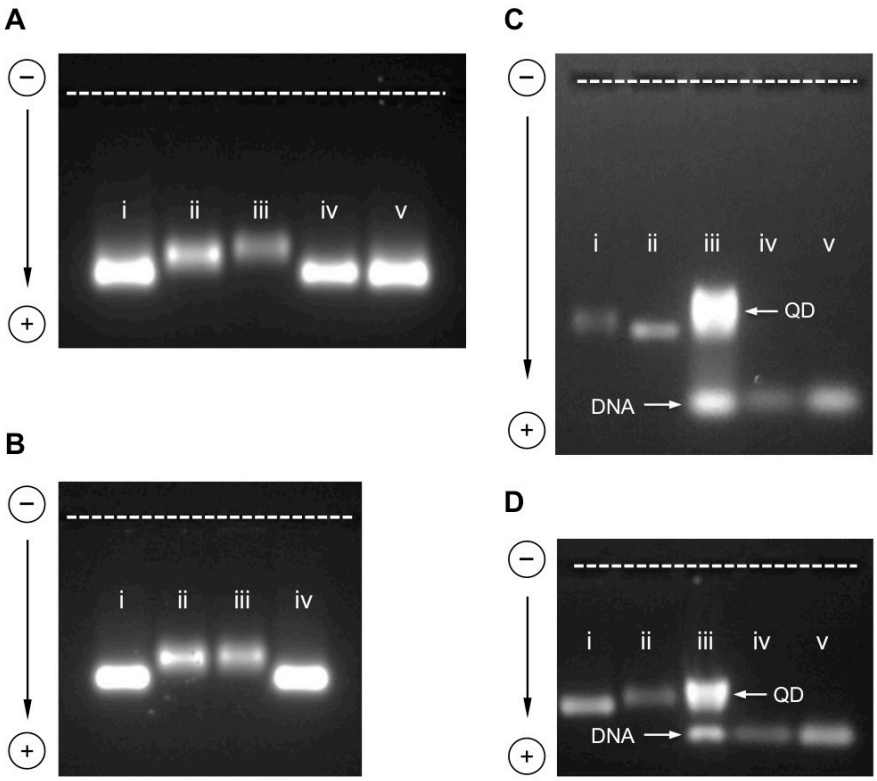

Figure 3.13 Agarose gel images of assembly of oligonucleotides onto the QDs. (A) PL image of an agarose gel showing the electrophoretic mobility of QD605–[Probe 1]–[Probe 2] conjugates: (i) $P_1 = P_2 = 0$; (ii) $P_1 = P_2 = 10$ with TCEP;(iii) $P_1 = P_2 = 15$ with TCEP; (iv) $P_1 = P_2 = 15$ without TCEP; (v) $P_1 = P_2 = 0$. Assembly is not 100% efficient (unlike polyhistidine terminated peptides, which approach 100% efficiency); (B) PL image of an agarose gel showing the electrophoretic mobilities for (i) $P_1 = P_2 = 0$; (ii) $P_1 = P_2 = 10$ (pre-salt aging); (iii) $P_1 = P_2 = 10$ (post-salt aging); (iv) $P_1 = P_2 = 0$. (C) PL images of an agarose gel stained with SYBR green for conjugate samples pre-salt aging: (i) QD605–[Probe 1] conjugates ($P = 10$); (ii) QD; (iii) QD605-[Probe 1] conjugates ($P = 10$) with Tgt 1 and SYBR green; (iv) 20% and (v) 40% Probe 1/Tgt 1 (no QD) with SYBR green. (D) PL images of an agarose gel stained with SYBR green for conjugate samples post-salt aging: (i) QD; (ii) QD605–[Probe 1] conjugates ($P = 10$); (iii) QD605–[Probe 1] conjugates ($P = 10$) with Tgt 1 and SYBR green; (iv) 20% and (v) 40% Probe 1/Tgt 1 (no QD) with SYBR green. Images in panels C and D were acquired with a color digital camera under long-wave UV light. The green channel was isolated in Image J for analysis. SYBR green and QD605 both give strong signals in the green channel. Reproduced from ref.[48] by permission of The Royal Society of Chemistry. Copyright 2016.

As shown in Table 2.2, probe oligonucleotide sequences Probe 1 and Probe 2 were 19 and 20 nt in length respectively, their respective partially complementary sequence were A633-labeled oligonucleotide sequence Blk 1(A633) with 14 nt in length, and A680-labeled oligonucleotide sequence Blk 2(A680), with 15 nt in length.

An experiment was done to assess the change in FRET efficiency, A633/QD605 and A680/QD605 PL ratios for two batches of QD605–[Probe 1]–[Probe 2], each with $P_1 = P_2 = P = 10$ or $P_1 = P_2 = P = 15$. As shown in Figure 3.14A and B, as the number of A633 or A680 per QD increases, the FRET efficiencies and A633/QD605 or A680/QD605 PL ratios for both batches increased and almost traced after each other until PL ratios saturate at a lower value of ~9 A633 (or A680) per QD for the batch of $P = 10$. For the batch of $P = 15$, A633/QD605 or A680/QD605 PL ratios saturate at a higher value of ~12 A633 (or A680) per QD.

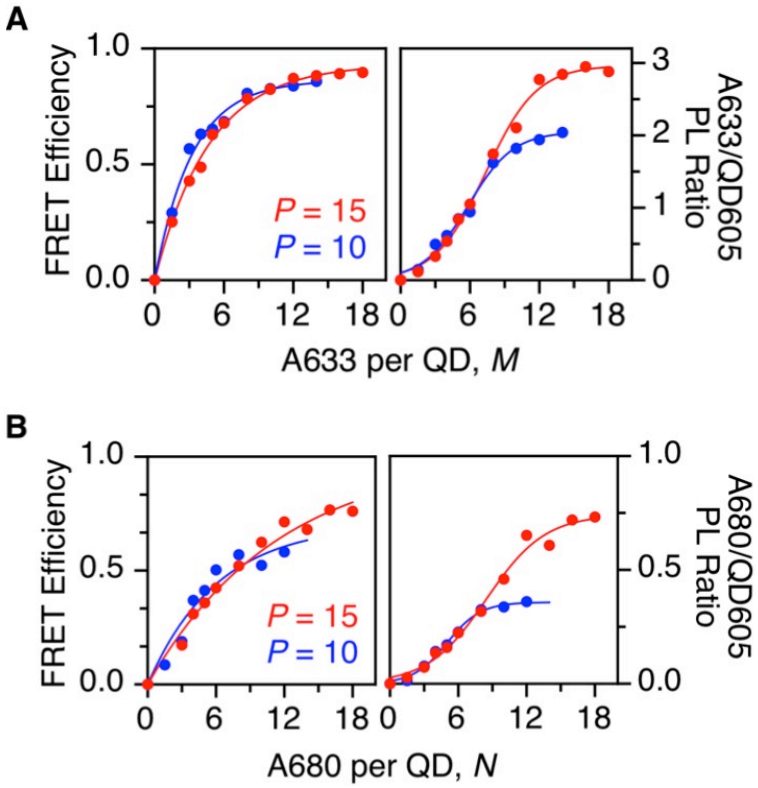

Figure 3.14 Changes in FRET efficiency and PL ratios with hybridization of QD605–[Probe 1]–[Probe 2] conjugates. (A) Hybridization with Blk 1(A633). (B) Hybridization with Blk 2(A680). Adapted from ref.[48] by permission of The Royal Society of Chemistry. Copyright 2016.

To illustrate the utility of QD605–[Probe 1]–[Probe 2] for cFRET configuration, different numbers of equivalents of Blk 1(A633) and Blk 2(A680) were hybridized with QD605–[Probe 1]–[Probe 2] as shown in Figure 3.15A. The samples were excited at 464 nm for recording PL spectra after ~30 min for hybridization to complete. As shown in Figure

3.15B–C, both of the QD605 quenching efficiency and A633/QD605 or A680/QD605 PL ratios increased as the number of equivalents of A633 or A680 increases. The quenching efficiency of QD, Q_{QD}, saturated as the number of dye-labeled block sequences approached seven. As an alternative to present data in Figure 3.15C, three-dimensional plots were constructed in Figure 3.16A–B, with number of A633 per QD (M) and A680 per QD (N) on the horizontal axes and the dye/QD PL ratios on the vertical axis. The trends in QD quenching efficiency and PL ratios presented by the oligonucleotide-linked cFRET configuration in Figure 3.15B–C were analogous to those of the peptide-linked configuration in Figure 3.7A (iii) inset and Figure 3.6B. These results demonstrated that the spectroscopic behavior of the oligonucleotide-linked cFRET configuration were similar to that of the peptide-linked configuration.

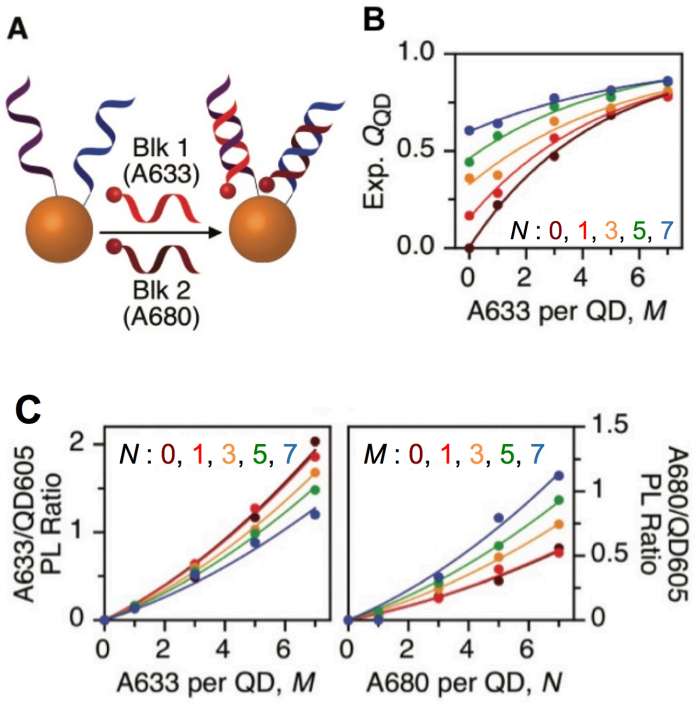

Figure 3.15 cFRET hybridization. (A) Schematic diagram. (B) Experimental Q_{QD} as a function of M and N. (C) Summary of the A633/QD605 and A680/ QD605 PL ratios as a function of M and N. The results are similar to those in Figure 3.6 and 3.7. Adapted from ref.[48] by permission of The Royal Society of Chemistry. Copyright 2016.

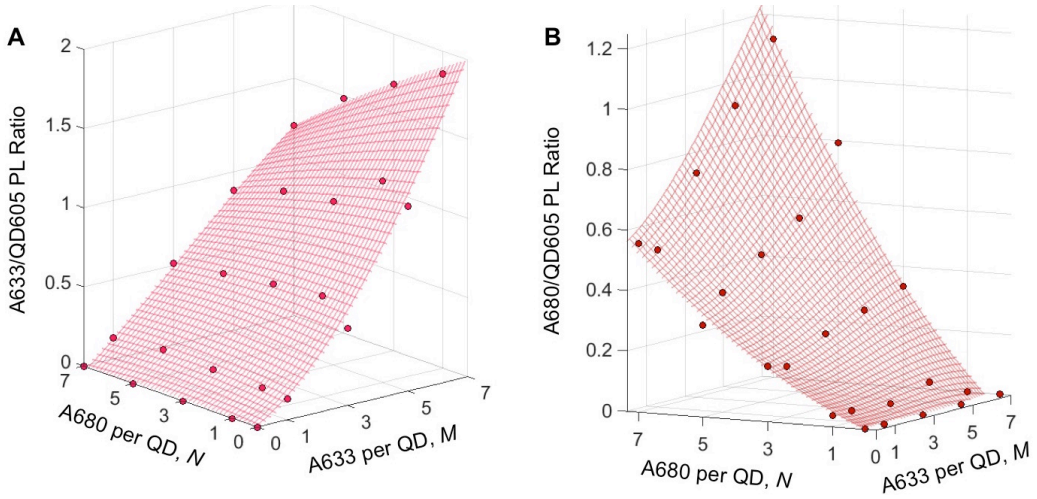

Figure 3.16 Three-dimensional plots of the calibration data in Figure 3.15C. (A) A633/QD605 PL ratio. (B) A680/QD605 PL ratio. Reproduced from ref.[48] by permission of The Royal Society of Chemistry. Copyright 2016.

Target displacement assay

To further demonstrate the utility of oligonucleotide-linked cFRET configuration for multiplexed hybridization assay, QD605–[Probe 1]–[Probe 2] (P_1 = P_2 = 10) was first hybridized with 10 equivalents of Blk 1(A633) and Blk 2(A680) each, and different number of equivalents of target strands Tgt 1 and Tgt 2 were added to displace dye-labeled block strands for loss of cFRET after 1 h (Figure 3.17A). These target strands are full-length complementary to the oligonucleotide probes assembled onto the QDs, and their hybridization with the probes strands was facilitated by the toeholds created by the shorter dye-labeled block strands (5 nucleotides less) than the probe strands. With loss of cFRET upon displacement assay, dye/QD PL ratios decreased as shown in Figure 3.17B, and such calibration curve could be used to correlate the A633/QD605 or A680/QD605 PL ratios with the number of equivalents of Tgt 1 and Tgt 2. As only 10 equivalents of each oligonucleotide probes were assembled onto the QDs, decrease in dye/QD PL ratios leveled off when around 8-10 equivalents of targets were added, with almost no change in dye/QD PL ratios from beyond 10 equivalents of target strands. A three-dimensional representation of the same data set is shown in Figure 3.18 A-B.

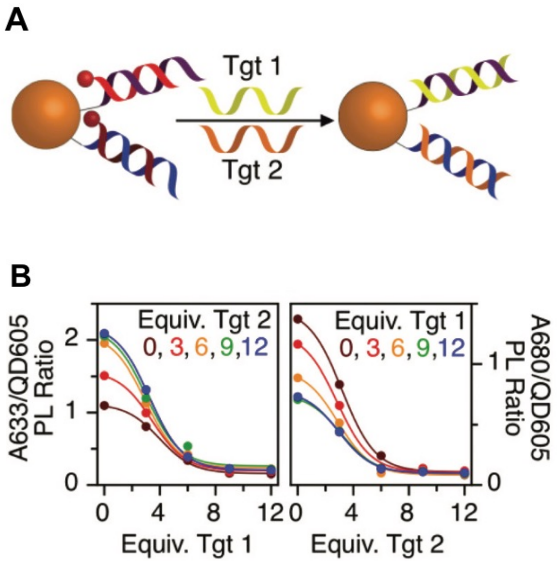

Figure 3.17 cFRET toehold-mediated strand displacement hybridization assay. (A) Schematic diagram. (B) Summary of the A633/QD605 and A680/QD605 PL ratios as a function of the number of equivalents of Tgt 1 and Tgt 2 added. Adapted from ref.[48] by permission of The Royal Society of Chemistry. Copyright 2016.

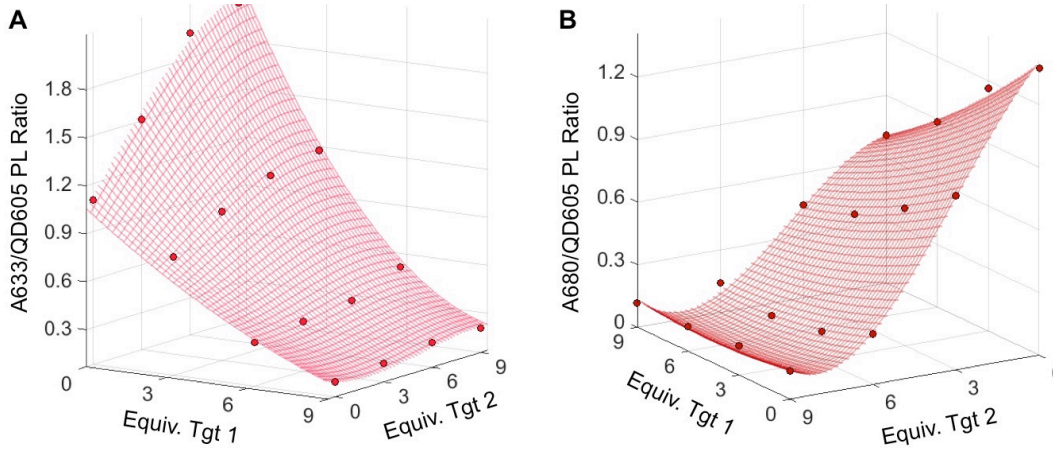

Figure 3.18 Three-dimensional plots of the calibration data in Figure 3.17B. (A) A633/QD605 PL ratio. (B) A680/QD605 PL ratio. The data was fit with polynomial surfaces to permit calculation of the number of equivalents of target in unknown samples from the measured PL ratios. Reproduced from ref.[48] by permission of The Royal Society of Chemistry.

To demonstrate the utility of these calibration plots for a multiplexed assay, the PL spectra of nine blinded unknown samples were measured. The corresponding A633/QD605 and A680/QD605 PL ratios, $\rho_{A633/QD}$ and $\rho_{A680/QD}$, were used to back-calculate the measured equivalents of Tgt 1 and Tgt 2 using calibration plots in Figure

3.18. The mathematical functions fitted to the calibration data for the displacement assay in Figure 3.18 (equivalent to data in Figure 3.17B, except showing only up to 9 equivalents of Tgt 1 or Tgt 2) are eqns. 3.3 and 3.4. A comparison between the actual and measured equivalents of Tgt 1 and Tgt 2 is drawn in Table 3.2. Most samples could be determined within an error range of ±1 equivalent of the actual value, except unknown samples 4 and 5, where the quantity of Tgt 2 could not be determined within an error arrange of ±1 equivalent of the actual value.

$$\rho_{A633/QD} = -5.52\times10^{-4}y^3 + 1.46\times10^{-3}x^2y + 9.95\times10^{-4}xy^2 + 4.48\times10^{-3}x^2 + 3.17\times10^{-4}y^2 - 3.31\times10^{-2}xy - 0.148x + 0.149y + 1.13 \quad (3.3)$$

$$\rho_{A680/QD} = 2.87\times10^{-3}y^3 - 7.06\times10^{-5}x^2y - 6.37\times10^{-4}xy^2 + 2.19\times10^{-3}x^2 - 2.50\times10^{-2}y^2 - 1.47\times10^{-2}xy - 9.65\times10^{-2}x - 0.147y + 1.40 \quad (3.4)$$

Table 3.2 Comparison between actual and measured equivalents of target 1 and target 2 in nine blinded unknown samples.

Unknown Sample	Actual Equivalent(s) of Target 1	Measured Equivalent(s) of Target 1	Actual Equivalent(s) of Target 2	Measured Equivalent(s) of Target 2
1	9	8.4	6	5.8
2	9	8.2	3	3.2
3	3	2.5	6	6.1
4	0	0	12	8.5[a]
5	0	0	6	9[a]
6	0	0	4.5	5.1
7	9	8.5	0	0
8	4.5	4.2	0	0.5
9	6	5.8	0	0.5

[a] Actual value falls outside the range of ±1 of the measured value.

3.2 Discussion

3.2.1 QD605–A633–A680 versus QD520–A555–A647

With the demonstration of feasibility to expand the idea of cFRET to other QDs and fluorescent dye combinations, it is interesting to delve into the optical properties of the fluorescent components of these combinations to gain insight into the functions and applications of the resulting cFRET configurations. Although cFRET has now been designed with more than one configuration using QDs and fluorescent dyes that perform at different regions of the UV-Vis spectrum, the design of cFRET is not trivial, but requires careful selection of fluorescent components. Important properties to consider for a cFRET configuration include common excitation minimum for both acceptor dyes, spectrally resolved emission between the three fluorescent components, spectral overlap of each donor-acceptor pair, large molar absorption coefficients and quantum yields of the fluorescent components.

Table 3.3 Optical properties of QD520–A555–A647 and QD605–A633–A680 cFRET configurations.

	QD520–A555–A647[32]	QD605–A633–A680
Diameter of QD core (nm)	3.6 ± 1.4	~4.8[5]
ε_{QD}[a] **(10^3 M^{-1} cm^{-1})**	57.8	232
ε_{A1}[a] **(10^3 M^{-1} cm^{-1})**	155	159
ε_{A2}[a] **(10^3 M^{-1} cm^{-1})**	270	183
$\lambda_{PL\ QD}$[b] **(nm)**	518	604
$\lambda_{PL\ A1}$[b] **(nm)**	566	648
$\lambda_{PL\ A2}$[b] **(nm)**	670	704
Φ_{QD}[c]	0.45	0.23
Φ_{A1}[c]	0.1	0.45
Φ_{A2}[c]	0.33	0.31
$J_{QD\text{-}A1}$[d] **(10^{-10} cm^6 mol^{-1})**	5.7	8.3
$J_{QD\text{-}A2}$[d] **(10^{-10} cm^6 mol^{-1})**	0.67	6.4
$J_{A1\text{-}A2}$[d] **(10^{-10} cm^6 mol^{-1})**	8.1	19

[a] Peak molar absorption coefficient. [b] Peak PL wavelength. [c] Quantum yield of the QD or dye-oligonucleotide conjugate. [d] Spectral overlap integral.

When compared to the previously well-studied cFRET configuration QD520–A555–A647, the long-wavelength configuration QD605–A633–A680 has analogous characteristics with some practical differences. An excitation minimum could be found for both dye acceptors in both cases. In QD520–A555–A647, an excitation minimum at ~400 nm is used to avoid direct excitation of the acceptor dyes, and an excitation minimum at longer wavelength (~464 nm) was used in the QD605–A633–A680 configuration for the same purpose. As QD520–A555–A647 has spectrally well resolved emission peaks that were ~50 nm (between QD520 and A555) and ~100 nm apart (between A555 and A647), the spectral separation between QD605, A633 and A680 were ~50 nm each. The same trends apply to the absorbance peaks for both configurations. The molar absorption coefficients of A555 (155,000 M^{-1} cm^{-1}) and A647 (270, 000 M^{-1} cm^{-1}) were similar in magnitude with A633 (159, 000 M^{-1} cm^{-1}) and A680 (183, 000 M^{-1} cm^{-1}).

All the above-mentioned optical properties act together resulting in differences in spectral overlap integrals of each FRET pair in both configurations, causing fundamental differences in rates of energy transfer. The spectral overlap integral for QD605–A633 (8.3×10^{-10} cm^6 mol^{-1}) FRET pair was almost 50% larger than that for QD520–A555 (5.7×10^{-10} cm^6 mol^{-1}). Such a large difference may be explained by the region of operation at longer wavelengths for QD605–A633–A680 configuration, since the spectral overlap integral is proportional to λ^4, as shown in eqn. 1.4. Besides the factor of longer-wavelength, the smaller spectral distance between the absorbance peaks of A633 and A680 than that of A555 and A647 results in much larger spectral overlap integrals in the QD605–A633–A680 configurations: 0.67×10^{-10} cm^6 mol^{-1} for QD520–A647 versus 6.4×10^{-10} cm^6 mol^{-1} for QD605–A680, and 8.1×10^{-10} cm^6 mol^{-1} for A555–A647 versus 19×10^{-10} cm^6 mol^{-1} for A633–A680.

The differences in magnitudes of spectral overlap integrals in both configurations result in differences of rates of energy transfer, as the rate of FRET, k_{FRET}, is proportional to the spectral overlap integral as suggested by eqn. 1.3. From the (M, 0) and (0, N) data sets as well as data of direct excitation of A633 in the cFRET configuration, the relative rates of energy transfer, $k_{D\text{-}A}k_D^{-1}$, of each of the pathways in QD605–A633–A680 cFRET

configuration are 0.34 (QD605–A633), 0.32 (QD605–A680) and 0.03 (A633–A680). Rates of both of the competitive pathways are comparable to each other, and they are ten-fold faster than the sequential pathway. The relative rates of energy transfer in QD520–A555–A647 configuration show much different contribution between the three FRET pathways. The QD520–A555 pathway, having a relative rate of energy transfer of 0.37, is much faster than the other two pathways, each at a relative rate of 0.09 (A555–A647) and 0.08 (QD520–A647). As suggested by these data, the smaller spectral separation between QD605 and A680 than that between QD520 and A647 renders a much faster competitive pathway in the QD605–A633–A680 cFRET configuration. Therefore, quenching of A633 was mainly due to its competition with A680 for energy from the QD605, while the quenching of A555 is almost evenly partitioned between the competitive and sequential pathways. The higher tendency for A680 to gain energy from the QD605 due to a faster relative rate of energy transfer induces a higher sensitivity of detection compared to the QD520–A647 FRET pair, as a change in quantity of analyte induces a larger change in the signal, in this case, the FRET efficiency and PL ratios.

The use of QD605–A633–A680 cFRET configuration also has the advantage of having much higher signal-to-background ratios in biological matrices such as serum and blood. This advantage is mainly due to the 20 times (or 5 times) larger molar absorption coefficient of the QD605 compared to QD520 (or QD525a) at its optimal excitation wavelength, leading to greater brightness in QD605. Two other factors that also improve S/B ratios in QD605–A633–A680 cFRET configuration include the reduction of background matrix autofluorescence at longer wavelengths and less attenuation of the excitation wavelength at 464 nm than 400 nm by the matrix.

As discussed in the previous section, A633 and A680 are less resistant to photobleaching than A647 even with the consideration of their excitation rates from the QD. Both acceptor dyes in the QD605–A633–A680 cFRET configuration are also susceptible to photobleaching versus only A647 in QD520–A555–A647, which renders QD520–A555–A647 a better choice for measurements with microscopes and low-background buffer sample matrices. On the other hand, the QD605–A633–A680 cFRET configuration would be a superior choice when discrete measurements (e.g. with plate reader) instead

of imaging with continuous illustration are made in samples with high-background biological sample matrices.

3.2.2 cFRET for oligonucleotides assays

Unlike peptides, which could be directly synthesized with polyhistidine for self-assembly, oligonucleotides were modified with a dithiol-terminated linker for assembly onto the QDs upon reduction. As discussed in Section 3.1.7, this assembly technique was not quantitative, and much less efficient than assembly via polyhistidine. Both gel images in Figure 3.13 and FRET data in Figure 3.14 suggest that the assembled oligonucleotide probes were always less than the number put in the mixture. When 15 oligonucleotides were added, 12 were assembled. When 10 were added, 9 were assembled. Therefore, for quantitative analysis, it is necessary to purify the QD-oligonucleotide probe conjugates from excess unassembled oligonucleotides through size exclusion chromatography. This process complicates the analysis process by diluting the concentration of the QD-oligonucleotide probe conjugates each time to different extents.

In contrast to the assembly of peptides, which have a smaller diameter of ~1.2 nm and with no strong electrostatic repulsion, the assembly of oligonucleotides faces the challenge of grouping multiple anionic polyphosphate DNA backbones of ~2 nm dia. onto the nanoparticle surface. To improve such assembly, the strategy of salt aging, which was frequently used with gold nanoparticles for oligonucleotides assembly, was applied here and achieved intended results.[53-55] A solution with high salt concentration brings large amount of mobile charge carriers (e.g. Na^+ and Cl^-) in vicinity of the anionic polyphosphate DNA backbones to screen negative charges for decreased electrostatic repulsion.

As QD605 at longer emission wavelength has larger size than QD520 as explained by the phenomenon of quantum confinement, the assembly of nucleotides potentially benefits from the use of QD605 instead of QD520, as larger surface area of QD605 would allow

more biomolecules to be assembled, especially for non-quantitative assembly such as dithiol-linker.

The design of the oligonucleotide-linked cFRET configuration has a few important features. Firstly, the acceptor dyes were located proximal to the QD, prior to the first nucleotide closest to the QD. Such design is different from previously reported FRET-based techniques for protease activity detection or target nucleotide sequence detection, where the dye acceptors were located distal to the QD. The proximal positions of acceptor dyes have the advantage of inducing more efficient FRET since the rate of FRET, k_{FRET}, is inversely proportional to the sixth power of the distance between any donor-acceptor FRET pair (eqn. 1.9). With more efficient FRET, the loss of acceptor dyes during target hybridization induces larger change in signal for increased sensitivity of detection. Secondly, compared to displacement of a block sequence destabilized by mismatch, toehold-mediated displacement at a site distal to the QD was more efficient. In a previously reported experiment, a QD-oligonucleotide probe was designed with 25 base-pairs in length and a dye-labeled block strand of 18 base-pairs in length with 3 mismatch was displaced by a target sequence of 98 base-pairs with full-length complementary target site facilitated by a 7 base-pairs toehold region proximal to the QD.[56] In this experiment, target strand was added in an excess of 5 equivalents to the QD-oligonucleotide probe to displace only 60% of block strands in 1 h, and the displacement assays did not reach equilibrium until beyond 5 h at room temperature.[56] In contrast, the toehold-mediated strand displacement of a 5 base-pairs shorter block oligonucleotide without mismatches from the QD-oligonucleotide probe by a full-length complementary sequence was efficient enough to reach equilibrium within 30 min for samples containing 3 to 12 equivalents of target strands relative to the QD-oligonucleotide probe conjugate. This is important for the purpose of quantitative analysis here, as the accuracy of quantification relies on a calibration plot constructed with samples of a range of equivalents of target strands compared to the QD-probe conjugate.

Quantification of both of Tgt 1 and Tgt 2 in 9 blinded unknown samples demonstrated the feasibility to use cFRET calibration plots for determining unknown within ± 1

equivalent except in two samples. These results summarized in Table 3.1 suggest minor limitations of using calibration plots in Figure 3.18 (or Figure 3.17B) for back-calculation of number of equivalents of Tgt 1 and Tgt 2. Since calibration plots were constructed with constraints from 0 to 9 for both Tgt 1 and Tgt 2, unknown sample that contained 12 equivalents of Tgt 2 (Sample 4) could not be quantified within error range of ±1 equivalent using such calibration. Another limitation of such calibration is the decreasing incremental change in PL ratios as more targets were added, resulting in decreasing sensitivity of detection (smaller change in signal in response to change in quantity of analyte). For example, in Figure 3.17B, increases in number of equivalents of Tgt 1 at a fixed number of equivalent of Tgt 2 decreases A680/QD605 PL ratio by decreasing the number of A633 per QD and recovering the QD PL. However, such change in A680/QD605 PL ratio ranges from ~0.7 when Tgt 2 = 0 to less than 0.05 when Tgt 2 = 9 as number of equivalents of Tgt 1 increases from 0 to 12. The almost 90% decrease in sensitivity makes it challenging to quantify Tgt 2 within a range of ±1 equivalent of the actual value in Sample 5 in Table 3.1, as A680/QD605 PL ratio changes only within a range of ~0.15 between 6 to 9 Tgt 2 (Figure 3.17B A680/QD605 PL ratio). On the other hand, quantification of 9 equivalents of Tgt 1 was achieved within ±1 range in Sample 7 due to the almost 3-fold larger range of A633/QD605 PL ratio as Tgt 1 increases from 6 to 9 equivalents (Figure 3.17B A633/QD605 PL ratio). Such limitation itself suggests that cFRET detection could be greatly improved in terms of sensitivity if a combination of QD and acceptor dyes are chosen such that the change in PL ratios are sufficiently large for a wider range of analyte quantity to be detected.

While quantitative analysis of targets at nanomolar concentrations was attempted with success in here, the limit of detection (LOD) may be pushed lower by decreasing the concentration of QD-probe conjugate. It has been suggested by previous studies that the dynamic range of detection in a FRET-based strategy has its upper limit scaled with the concentration of the QD-probe conjugate, and its LOD being a function of the amount of QD-probe conjugate. [43] An instrument with high sensitivity would assist in low LOD with decreased QD-probe conjugate concentration. The LOD is defined as three standard

deviations above the baseline of detection when no targets are present, the degree of instrumental noise also plays an important role.[43]

Chapter 4
Conclusion

In conclusion, a new long-wavelength cFRET configuration QD605–A633–A680 was designed, and this new configuration was used to demonstrate the first cFRET-based DNA assays with successful simultaneous quantification of two unlabeled target strands.

The photophysics of the QD605–A633–A680 cFRET configuration were characterized in terms of its energy transfer pathways, and its susceptibility to photobleaching was assessed through a peptide-linked QD605–A633–A680 cFRET configuration. Although the characterization of competitive and sequential energy transfer pathways of this new cFRET configuration suggested it obeyed the conventional FRET formalism, the balance between the competitive and sequential FRET pathways was found to be different from the conventional green cFRET configuration. By comparison to the conventional green cFRET configuration QD520–A555–A647, the long-wavelength cFRET configuration QD605–A633–A680 had superior brightness and signal-to-background ratios in biological samples such as serum and blood media. However, a drawback is that it is more susceptible to photobleaching.

For demonstration of utility of this new cFRET configuration, an oligonucleotide-linked QD605–A633–A680 cFRET configuration was constructed for multiplexed quantification of two unlabeled target strands through efficient toehold-mediated strand displacement assays. Unknown quantities of two target strands were successfully determined in seven out of nine blinded unknown samples, and sixteen out of eighteen test samples were successfully quantified within an error range of ±1 equivalent. Overall, this long-wavelength cFRET configuration has shown certain important improvements compared to the conventional configuration, and found itself a superior strategy in certain applications where the conventional configuration failed to deliver satisfactory results.

There are many prospective applications of long-wavelength cFRET that a worth exploring in future work. One is taking long-wavelength cFRET strategy into cells for detection of enzymatic activities or DNA/RNA within cells. The great brightness of QDs in this new strategy as well as the minimization of cellular autofluorescence due to its

red-shift in excitation render it a great tool for single particle tracking in imaging of cells if alternative acceptor dyes could be found with higher resistance to photobleaching. In terms of improving the quality of detection, lower detection limit could be attempted by scaling down the concentration of QD-probe conjugates. Overall, this new promising strategy of long-wavelength cFRET adds valuable alternative to existing FRET-based bioanalysis.

References

1. Penn, S.G., L. He, and M.J. Natan, *Nanoparticles for bioanalysis.* Current Opinion in Chemical Biology, 2003. **7**(5): p. 609-615.
2. Algar, W.R., et al., *Semiconductor Quantum Dots in Bioanalysis: Crossing the Valley of Death.* Analytical Chemistry, 2011. **83**(23): p. 8826-8837.
3. Petryayeva, E., W.R. Algar, and I.L. Medintz, *Quantum Dots in Bioanalysis: A Review of Applications Across Various Platforms for Fluorescence Spectroscopy and Imaging.* Applied Spectroscopy, 2013. **67**(3): p. 215-252.
4. Bera, D., et al., *Quantum Dots and Their Multimodal Applications: A Review.* Materials, 2010. **3**(4): p. 2260-2345.
5. Medintz, I.L., et al., *Quantum dot bioconjugates for imaging, labelling and sensing.* Nature Materials, 2005. **4**(6): p. 435-446.
6. Chan, W.C.W. and S.M. Nie, *Quantum dot bioconjugates for ultrasensitive nonisotopic detection.* Science, 1998. **281**(5385): p. 2016-2018.
7. Mattoussi, H., et al., *Self-assembly of CdSe-ZnS quantum dot bioconjugates using an engineered recombinant protein.* Journal of the American Chemical Society, 2000. **122**(49): p. 12142-12150.
8. Jin, T., et al., *A quantum dot-based ratiometric pH sensor.* Chemical Communications, 2010. **46**(14): p. 2408-2410.
9. Susumu, K., B.C. Mei, and H. Mattoussi, *Multifunctional ligands based on dihydrolipoic acid and polyethylene glycol to promote biocompatibility of quantum dots.* Nature Protocols, 2009. **4**(3): p. 424-436.
10. Breus, V.V., et al., *Zwitterionic Biocompatible Quantum Dots for Wide pH Stability and Weak Nonspecific Binding to Cells.* Acs Nano, 2009. **3**(9): p. 2573-2580.
11. Muro, E., et al., *Small and Stable Sulfobetaine Zwitterionic Quantum Dots for Functional Live-Cell Imaging.* Journal of the American Chemical Society, 2010. **132**(13): p. 4556-+.
12. Kim, S. and M.G. Bawendi, *Oligomeric Ligands for luminescent and stable nanocrystal quantum dots.* Journal of the American Chemical Society, 2003. **125**(48): p. 14652-14653.
13. Zhang, Y.J. and A. Clapp, *Overview of Stabilizing Ligands for Biocompatible Quantum Dot Nanocrystals.* Sensors, 2011. **11**(12): p. 11036-11055.
14. Liu, Y.C., et al., *Highly luminescent, stable, and water-soluble CdSe/CdS core - Shell dendron nanocrystals with carboxylate anchoring groups.* Langmuir, 2006. **22**(14): p. 6341-6345.
15. Skaff, H. and T. Emrick, *The use of 4-substituted pyridines to afford amphiphilic, pegylated cadmium selenide nanoparticles.* Chemical Communications, 2003(1): p. 52-53.
16. Yu, W.W., et al., *Forming biocompatible and nonaggregated nanocrystals in water using amphiphilic polymers.* Journal of the American Chemical Society, 2007. **129**(10): p. 2871-2879.
17. Dubertret, B., et al., *In vivo imaging of quantum dots encapsulated in phospholipid micelles.* Science, 2002. **298**(5599): p. 1759-1762.

18. Algar, W.R., et al., *The Controlled Display of Biomolecules on Nanoparticles: A Challenge Suited to Bioorthogonal Chemistry.* Bioconjugate Chemistry, 2011. **22**(5): p. 825-858.
19. Irrgang, J., et al., *Analysis of Non-Covalent Bioconjugation of Colloidal Nanoparticles by Means of Atomic Force Microscopy and Data Clustering.* Chemphyschem, 2009. **10**(9-10): p. 1483-1491.
20. Delehanty, J.B., et al., *Self-assembled quantum dot-peptide bioconjugates for selective intracellular delivery.* Bioconjugate Chemistry, 2006. **17**(4): p. 920-927.
21. Medintz, I.L., et al., *Multiplex Charge-Transfer Interactions between Quantum Dots and Peptide-Bridged Ruthenium Complexes.* Analytical Chemistry, 2009. **81**(12): p. 4831-4839.
22. Cui, B.X., et al., *One at a time, live tracking of NGF axonal transport using quantum dots.* Proceedings of the National Academy of Sciences of the United States of America, 2007. **104**(34): p. 13666-13671.
23. Fichter, K.M., et al., *Kinetics of G-protein-coupled receptor endosomal trafficking pathways revealed by single quantum dots.* Proceedings of the National Academy of Sciences of the United States of America, 2010. **107**(43): p. 18658-18663.
24. Skoog, D.A., F.J. Holler, and S.R. Crouch, *Principles of instrumental analysis*. 6th ed. 2007, Belmont, CA: Thomson Brooks/Cole. xv, 1039 p.
25. Medintz, I.L. and H. Mattoussi, *Quantum dot-based resonance energy transfer and its growing application in biology.* Physical Chemistry Chemical Physics, 2009. **11**(1): p. 17-45.
26. Pons, T., et al., *On the quenching of semiconductor quantum dot photoluminescence by proximal gold nanoparticles.* Nano Letters, 2007. **7**(10): p. 3157-3164.
27. Allan, G. and C. Delerue, *Energy transfer between semiconductor nanocrystals: Validity of Forster's theory.* Physical Review B, 2007. **75**(19): p. 8.
28. Curutchet, C., et al., *Examining Forster energy transfer for semiconductor nanocrystalline quantum dot donors and acceptors.* Journal of Physical Chemistry C, 2008. **112**(35): p. 13336-13341.
29. Algar, W.R., et al., *Emerging non-traditional Forster resonance energy transfer configurations with semiconductor quantum dots: Investigations and applications.* Coordination Chemistry Reviews, 2014. **263**: p. 65-85.
30. Resch-Genger, U., et al., *Quantum dots versus organic dyes as fluorescent labels.* Nature Methods, 2008. **5**(9): p. 763-775.
31. Clapp, A.R., et al., *Fluorescence resonance energy transfer between quantum dot donors and dye-labeled protein acceptors.* Journal of the American Chemical Society, 2004. **126**(1): p. 301-310.
32. Wu, M., et al., *Energy Transfer Pathways in a Quantum Dot-Based Concentric FRET Configuration.* Journal of Physical Chemistry C, 2015. **119**(46): p. 26183-26195.
33. Massey, M., J.J. Li, and W.R. Algar, *Multifunctional Concentric FRET-Quantum Dot Probes for Tracking and Imaging of Proteolytic Activity.* Methods in molecular biology (Clifton, N.J.), 2017. **1530**: p. 63-97.

34. Algar, W.R., et al., *Assembly of a Concentric Forster Resonance Energy Transfer Relay on a Quantum Dot Scaffold: Characterization and Application to Multiplexed Protease Sensing.* Acs Nano, 2012. **6**(12): p. 11044-11058.
35. Saiki, R.K., et al., *ENZYMATIC AMPLIFICATION OF BETA-GLOBIN GENOMIC SEQUENCES AND RESTRICTION SITE ANALYSIS FOR DIAGNOSIS OF SICKLE-CELL ANEMIA.* Science, 1985. **230**(4732): p. 1350-1354.
36. Saghatelian, A., et al., *DNA detection and signal amplification via an engineered allosteric enzyme.* Journal of the American Chemical Society, 2003. **125**(2): p. 344-345.
37. Park, S.J., T.A. Taton, and C.A. Mirkin, *Array-based electrical detection of DNA with nanoparticle probes.* Science, 2002. **295**(5559): p. 1503-1506.
38. Cederquist, K.B., R.S. Golightly, and C.D. Keating, *Molecular beacon-metal nanowire interface: Effect of probe sequence and surface coverage on sensor performance.* Langmuir, 2008. **24**(16): p. 9162-9171.
39. Wang, J., D.K. Xu, and R. Polsky, *Magnetically-induced solid-state electrochemical detection of DNA hybridization.* Journal of the American Chemical Society, 2002. **124**(16): p. 4208-4209.
40. Suzuki, M., et al., *Quantum dot FRET Biosensors that respond to pH, to proteolytic or nucleolytic cleavage, to DNA synthesis, or to a multiplexing combination.* Journal of the American Chemical Society, 2008. **130**(17): p. 5720-5725.
41. Huang, S., et al., *A Simple QD-FRET Bioprobe for Sensitive and Specific Detection of Hepatitis B Virus DNA.* Journal of Fluorescence, 2013. **23**(5): p. 1089-1098.
42. Zhang, C.Y., et al., *Single-quantum-dot-based DNA nanosensor.* Nature Materials, 2005. **4**(11): p. 826-831.
43. Algar, W.R. and U.J. Krull, *Towards multi-colour strategies for the detection of oligonucleotide hybridization using quantum dots as energy donors in fluorescence resonance energy transfer (FRET).* Analytica Chimica Acta, 2007. **581**(2): p. 193-201.
44. Zhang, C.Y. and J. Hu, *Single Quantum Dot-Based Nanosensor for Multiple DNA Detection.* Analytical Chemistry, 2010. **82**(5): p. 1921-1927.
45. Algar, W.R. and U.J. Krull, *Multiplexed Interfacial Transduction of Nucleic Acid Hybridization Using a Single Color of Immobilized Quantum Dot Donor and Two Acceptors in Fluorescence Resonance Energy Transfer.* Analytical Chemistry, 2010. **82**(1): p. 400-405.
46. Wu, M., E. Petryayeva, and W.R. Algar, *Quantum Dot-Based Concentric FRET Configuration for the Parallel Detection of Protease Activity and Concentration.* Analytical Chemistry, 2014. **86**(22): p. 11181-11188.
47. Wu, M. and W.R. Algar, *Concentric Forster Resonance Energy Transfer Imaging.* Analytical Chemistry, 2015. **87**(16): p. 8078-8083.
48. Li, J.J. and W.R. Algar, *A long-wavelength quantum dot-concentric FRET configuration: characterization and application in a multiplexed hybridization assay.* Analyst, 2016. **141**(12): p. 3636-3647.
49. Li, J.J., et al., *Large-scale synthesis of nearly monodisperse CdSe/CdS core/shell nanocrystals using air-stable reagents via successive ion layer adsorption and reaction.* Journal of the American Chemical Society, 2003. **125**(41): p. 12567-12575.

50. Yu, W.W. and X.G. Peng, *Formation of high-quality CdS and other II-VI semiconductor nanocrystals in noncoordinating solvents: Tunable reactivity of monomers.* Angewandte Chemie-International Edition, 2002. **41**(13): p. 2368-2371.
51. Algar, W.R. and U.J. Krull, *Interfacial Chemistry and the Design of Solid-Phase Nucleic Acid Hybridization Assays Using Immobilized Quantum Dots as Donors in Fluorescence Resonance Energy Transfer.* Sensors, 2011. **11**(6): p. 6214-6236.
52. Umberger, J.Q. and V.K. Lamer, *THE KINETICS OF DIFFUSION CONTROLLED MOLECULAR AND IONIC REACTIONS IN SOLUTION AS DETERMINED BY MEASUREMENTS OF THE QUENCHING OF FLUORESENCE.* Journal of the American Chemical Society, 1945. **67**(7): p. 1099-1109.
53. Shi, D.W., et al., *A facile and efficient method to modify gold nanorods with thiolated DNA at a low pH value.* Chemical Communications, 2013. **49**(25): p. 2533-2535.
54. Wang, R.S., I. Bowling, and W.Y. Liu, *Cost effective surface functionalization of gold nanoparticles with a mixed DNA and PEG monolayer for nanotechnology applications.* Rsc Advances, 2017. **7**(7): p. 3676-3679.
55. Zhang, X., M.R. Servos, and J.W. Liu, *Instantaneous and Quantitative Functionalization of Gold Nanoparticles with Thiolated DNA Using a pH-Assisted and Surfactant-Free Route.* Journal of the American Chemical Society, 2012. **134**(17): p. 7266-7269.
56. Vannoy, C.H., et al., *A competitive displacement assay with quantum dots as fluorescence resonance energy transfer donors.* Analytica Chimica Acta, 2013. **759**: p. 92-99.